

GALAXY ZOO: MORPHOLOGICAL CLASSIFICATIONS FOR 150,000 GALAXIES IN HST LEGACY IMAGING

KYLE W. WILLETT^{1,2}, MELANIE A. GALLOWAY¹, CHRIS J. LINTOTT³, B.D. SIMMONS^{3,4,5,6}, KAREN L. MASTERS^{7,8}, TOM MELVIN⁷, STEVEN P. BAMFORD⁹, EDWARD M. EDMONDSON⁷, LUCY F. FORTSON¹, KEVIN SCHAWINSKI¹⁰, EDMOND CHEUNG¹¹, CLAUDIA SCARLATA¹, MELANIE BECK¹, ARFON M. SMITH^{3,12,13}, MICHAEL PARRISH¹², ROGER L. GRIFFITH^{14,15}, ANNA HAN¹⁶

ABSTRACT

We present the data release paper for the Galaxy Zoo: Hubble (GZH) project.^a This is the third phase in a large effort to measure reliable morphologies of galaxies on detailed scales by using crowd-sourced visual classifications of color composite image. Images in GZH are selected from various *Hubble Space Telescope* Legacy programs using the Advanced Camera for Surveys (AEGIS, COSMOS, GEMS, GOODS-N, and GOODS-S), with filters selected to probe the rest-frame optical emission from galaxies out to $z \simeq 1$. The galaxies selected for GZH classifications go down to magnitude limits of $m_I < 23.5$ and have a median redshift of $\langle z \rangle = 0.9 \pm 0.6$, with a tail extending out to $z \simeq 4$. The GZH morphological data includes measurements of both bulge- and disk-dominated galaxies, details on spiral disk structure that relate to the Hubble type, and numerous measurements of clump identification and geometry. This paper also describes and employs a novel method for calibrating morphological bias by using artificially-redshifted galaxy images as a baseline. This paper presents both the raw and calibrated morphological vote fractions for 150,771 galaxies, constituting a large data set suitable for large-scale studies of galaxy evolution.

Keywords: galaxies:structure — galaxies:high redshift — galaxies:evolution — methods:data analysis — catalogs

1. INTRODUCTION

The morphology of galaxies encodes information on the orbital parameters and assembly history of the contents, including gas, dust, stars, and the central black hole. The morphology is also closely related to the local environment of the galaxy, as mutual interactions such as gravitational tides, shocks in cluster environments and direct mergers can all change the shape of the galaxy's potential. For M^* galaxies in the local Universe, this typically manifests at the most basic level as the difference between bulge-dominated, virialized systems resembling ellipticals (early-types) and disk-dominated, rotationally-supported disks (late-types) frequently exhibiting spiral arms. This dichotomy has been used to explore much of the astrophysics encoding galaxy formation and evolution, and has been shown to be closely linked with other galactic properties such as stellar mass, halo mass, bolometric luminosity, black hole activity, effective radius, and the relative ages of the stellar populations.

The advent of larger telescopes in an increasing range of observable wavelengths has revealed that the distribution and properties of galaxy morphology have strongly evolved over the lifetime of the Universe. At redshift $z \simeq 1$ (roughly 6 Gyr after the Big Bang), many galaxies are still in the process of assembling the baryonic mass required to reproduce the structures seen in the present day. This occurs in a variety of pathways, including accretion of baryons from large-scale galactic filaments onto halos via streaming, mergers of individual dark matter halos along with their baryons, conversion of gas into stars via gravitational collapse and star formation, etc. The process can also be slowed or even reversed via feedback from stellar winds, supernovae, and active black holes. Each of these processes affects on the galaxy morphology, and so an accurate measurement of the demographics as a function of redshift provides an extremely powerful observational constraint on the physics involved (for a recent review see Conselice 2014).

Theoretical predictions for the morphology of galaxies as a function of redshift are primarily computed within the Λ CDM cosmological framework. Full treatments of this model gravitational interactions between baryons and dark matter, hydrodynamics of the gas, and baryonic physics related to star formation and evo-

^a This publication has been made possible by the participation of more than 200,000 volunteers in the Galaxy Zoo project. Their contributions are individually acknowledged at <http://authors.galaxyzoo.org/authors.html>.

lution. The most advanced simulations now include volumes up to $\sim 100 \text{ Mpc}^3$ while simultaneously resolving the smaller scales necessary to reproduce the baryonic physics (Vogelsberger et al. 2014; Schaye et al. 2015). Such simulations predict clustering of galaxies on large scales in a hierarchical assembly model (Silk & Mamon 2012). The structure of individual galaxies is affected by the merger history (Toomre & Toomre 1972; Hopkins et al. 2010), local environment (such as the morphology-density relation; Dressler 1980), initial dark halo mass, and many other factors. Morphologies of individual simulated high-mass galaxies at $z \sim 2 - 3$ commonly show kpc-scale “clumpy” structures and few galaxies that are either smooth or well-ordered spirals; asymmetric profiles with strong density constraints dominate populations in the early Universe until at least $z \sim 1$ (Genel et al. 2014).

Observational studies of galaxies at high-redshift also display a wide range of morphological types, many of which are rare or absent at $z \sim 0$. These include spheroids and disks (akin to the ellipticals/spirals seen in the local Universe), but also a significant population of massive, more irregular galaxies, including mergers, tadpoles, chains, double-clumps, and clump-clusters (Elmegreen et al. 2005, 2007; Cameron et al. 2011; Förster Schreiber et al. 2011; Kartaltepe et al. 2015). In contrast, while grand-design spirals have been observed as far back as $z = 2.18$ (Law et al. 2012a), their spatial density suggests that they are exceedingly rare, with a very low overall disk fraction (Mortlock et al. 2013). Current observational data thus strongly suggests that the classical Hubble sequence/tuning fork (Hubble 1936) is not a suitable framework for characterizing high-redshift morphology.

Space-based observatories, particularly the *Hubble Space Telescope*, have been responsible for the bulk of imaging studies of high-redshift galaxies. Observations of fixed fields with very deep imaging (eg, Williams et al. 1996; Giavalisco et al. 2004; Beckwith et al. 2006; Davis et al. 2007; Scoville et al. 2007; Grogin et al. 2011) give the photometric sensitivity necessary to detect L^* galaxies at $z > 1$, while also providing the angular resolution to distinguish internal structure and characterize the morphology. While these measurements are helped by the fact that the angular diameter distance is relatively flat at $z > 1$ in a flat ΛCDM cosmology, the scales are only of the order $\sim 5 - 10 \text{ kpc}/''$ (Wright 2006). *HST* can thus resolve much of the structure for a Milky Way-sized galaxy (at least for distinguishing a disk from a bulge), but will be limited for more compact structures. Since the size of galaxies evolves as roughly $r \propto (1+z)^{-1}$ (Law et al. 2012b), the more compact sizes of earlier galaxies make detailed morphologies a challenge even for *HST* (Chevance et al. 2012). The

public availability of more than 10^5 galaxies in archival imaging across various studies gives a data sample with the potential for high statistical significance.

One of the major difficulties in studying the morphologies of galaxies in large samples lies in the system of measurement. Visual classification by experts has been used for many years (eg, Hubble 1926; de Vaucouleurs 1959; Sandage 1961; van den Bergh 1976; Nair & Abraham 2010; Baillard et al. 2011; Kartaltepe et al. 2015). These methods have advantages in using the significant processing power of the human brain to identify patterns, but suffer from issues such as lack of scaling to large surveys and potential issues with replicability and calibration. Automated measurements, both parametric (Peng et al. 2002; Simard et al. 2011; Lackner & Gunn 2012) and non-parametric (Abraham et al. 2003; Conselice 2003; Lotz et al. 2004; Scarlata et al. 2007; Bamford et al. 2008; Freeman et al. 2013), scale well to arbitrary sample sizes, but do not always fully capture the relevant features, especially for asymmetric galaxies that become increasingly common at high redshifts. The Galaxy Zoo project (Lintott et al. 2008, 2011) utilizes crowdsourced visual classifications to measure galaxies in color-composite images. With $> 2 \times 10^5$ classifiers, this allows for multiple independent classifications of each image which are combined and calibrated to give a distribution of vote fractions proportional to the probability of a feature being visible. While the crowdsourced data require extensive calibration (Bamford et al. 2009; Willett et al. 2013), they have a proven reliability and have been used in dozens of papers (eg, Land et al. 2008; Bamford et al. 2009; Darg et al. 2010; Masters et al. 2011; Skibba et al. 2012; Simmons et al. 2013; Schawinski et al. 2014; Willett et al. 2015).

This paper presents the results from the Galaxy Zoo Hubble (GZH) project.¹ GZH was the third phase of Galaxy Zoo, following its initial results classifying $\sim 900,000$ SDSS images into primarily early/late types (Lintott et al. 2011) and Galaxy Zoo 2, which covered $\sim 250,000$ SDSS images using a more detailed classification scheme that included bars, spiral arms, and galactic bulges (Willett et al. 2013). GZH used a similarly detailed classification scheme, but focused for the first time on images of high-redshift galaxies taken with the *Hubble Space Telescope*.

The sample selection and creation of the images used for GZH is described in Section 2. Section 3 describes the GZH interface and the collection of classifications. Section 4 outlines the process used to calibrate and “debias” the crowdsourced votes. Section 5 gives the main

¹ <http://zoo3.galaxyzoo.org/>

results as a catalog, with several examples of how the data may be queried in Section 6. Section 7 gives a short overview of the observed morphological demographics and compares them to several other catalogs, with a summary in Section 8.

This paper uses the WMAP9 cosmology parameters of $(\Omega_m, \Omega_\Lambda, h) = (0.258, 0.718, 0.697)$ (Hinshaw et al. 2013).

2. SAMPLE AND DATA

2.1. *Hubble Legacy Surveys*

The GZH project contains images drawn from a number of different dedicated surveys and sample selection criteria. The majority of the data (as implied by the project name) are taken directly from *HST* Legacy Surveys, all of which primarily use imaging from the Advanced Camera for Surveys (ACS). Results from the individual surveys have been combined into a single photometric and morphological database, the Advanced Camera for Surveys General Catalog (ACS-GC; Griffith et al. 2012). A summary of the key parameters is given in Table 1.

- The All-Wavelength Extended Groth Strip International Survey (AEGIS; Davis et al. 2007) covers a strip centered at $\alpha = 14^{\text{h}}17^{\text{m}}$, $\delta = +52^\circ30'$. This area was selected for a deep survey due to a combination of low extinction and low Galactic/zodiacal emission. The ACS images covered 63 separate tiles over a total area of ~ 710 arcmin 2 . The two ACS bands for AEGIS had exposure times of 2300 seconds in F606W (V_{606W}) and 2100 seconds in F814W (I_{814W}). The final mosaic images are dithered to a resolution of 0.03 ''/pixel. For extended objects, the limiting magnitudes of sources in AEGIS are 26.23 (AB) in V_{606W} and 25.61 (AB) in I_{814W} .
- The Great Observatories Origins Deep Survey (GOODS; Giavalisco et al. 2004) covers two separate fields in the northern and southern hemispheres: the Hubble Deep Field-North ($\alpha = 12^{\text{h}}36^{\text{m}}$, $\delta = +62^\circ14'$) and the Chandra Deep Field-South ($\alpha = 03^{\text{h}}32^{\text{m}}$, $\delta = -27^\circ48'$). The *HST* ACS imaging data from the two fields are referred to as GOODS-N and GOODS-S, respectively. ACS imaging in GOODS fields used 4 filters – F435W (B_{435W}), V_{606W} , F775W (I_{775W}), and F850LP (I_{850LP}). The mean exposure times for each epoch vary by band, from 1050–2100 seconds. The B_{435W} images were completed in a single epoch at the beginning of the survey, but the V_{606W} , I_{775W} , and I_{850LP} images were taken in five separate epochs separated by 40–50 days each. Images are dithered to a pixel

scale of 0.03 ''/pixel and cover a total area of ~ 320 arcmin 2 (160 arcmin 2 per north/south field). The 5σ limiting magnitudes for extended sources are 25.7 for V_{606W} and 25.0 for I_{775W} .

- The Cosmic Evolution Survey (COSMOS; Scoville et al. 2007) covers an area of ~ 1.8 deg 2 centered at $\alpha = 10^{\text{h}}00^{\text{m}}$, $\delta = +02^\circ12'$. Its location near the celestial equator was designed to enable coverage by ground-based telescopes in both the Northern and Southern Hemispheres, in addition to space-based observatories. The ACS data for COSMOS consists of 1 orbit per pointing with an exposure time of 2028 seconds in I_{814W} ; 590 total pointings are used to cover the entire field. The image resolution is dithered to 0.05 ''/pixel. The 50% completeness magnitude for a galaxy with a half-light radius of 0.50'' in I_{814W} is 24.7 mag.
- The Galaxy Evolution from Morphologies and SEDs (GEMS; Rix et al. 2004; Caldwell et al. 2008) survey is also centered on the Chandra Deep Field-South. The GEMS data covers ~ 800 arcmin 2 , completely surrounding the area covered by GOODS-S. Images from ACS in GEMS have 1 orbit per pointing for a total of 63 pointings. The exposure times are 2160 and 2286 seconds in V_{606W} and I_{850LP} , respectively. The image resolution has a pixel scale of 0.03 ''/pixel. The 5σ limiting magnitudes for source detection are 25.7 AB in V_{606W} and 24.2 AB in I_{850LP} .

2.2. *Galaxy selection*

In the ACS-GC (Griffith et al. 2012), individual galaxies are identified using a combination of SExtractor (Bertin & Arnouts 1996) and the galaxy-profile fitting framework GALAPAGOS (Barden et al. 2012). GZH includes all galaxies with $m < 23.5$, where m is in the I_{814W} , I_{850LP} , or I_{775W} for the AEGIS + COSMOS, GEMS + GOODS-S, and GOODS-N surveys, respectively. This yielded a total of 113,166 images (Table 1).

Single-epoch images from SDSS Stripe 82 were selected using the same criteria from Willett et al. (2013), which required limits of $\text{petroR90_r} > 3''$ (where petroR90_r is the radius containing 90% of the r' Petrosian flux) and a magnitude brighter than $m_r < 17.77$. 21,522 galaxies in SDSS met these criteria. Coadded images from Stripe 82 were selected from the union of galaxies with coadded magnitudes brighter than 17.77 mag and the galaxies detected in the single-depth images and matched to a coadd source. This resulted in a larger set of 30,339 images. Of the images in the coadded sample, 5144 (17 percent) are dimmer than the initial magnitude cut of 17.77.

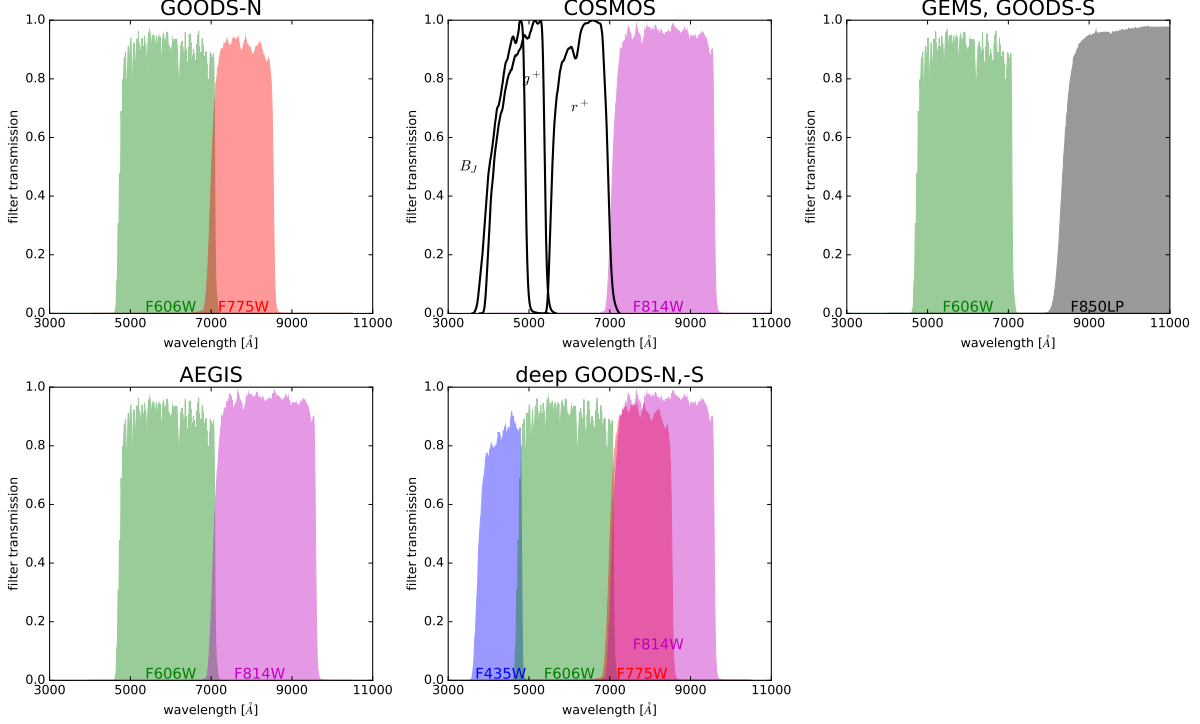


Figure 1. Transmission curves of the filters used by *HST* Advanced Camera for Surveys (ACS) in wide-field channel mode for the various surveys in Galaxy Zoo: Hubble. The unfilled black curves show the filters for the Suprime Camera on the *Subaru* telescope which were used to create color gradients in the composite images for COSMOS.

Table 1. Summary of Galaxy Zoo: Hubble imaging

Survey	t_{exp} [sec]	Filters	Resolution ["/pix]	Area [arcmin 2]	N_{galaxies}
AEGIS	2100–2300	V_{606W} and I_{814W}	0.03	710	8157
COSMOS	2028	I_{814W}	0.05	6480	88530
GEMS	2160–2286	V_{606W} and I_{850LP}	0.03	800	9143
GOODS	1000–2100	B_{435W} , V_{606W} , I_{775W} , I_{850LP}	0.03	320	7336
<i>GOODS-N</i>	—	—	—	—	2551
<i>GOODS-S</i>	—	—	—	—	4785
total	—	—	—	8310	113166

2.3. Image creation

The images used for classification in GZH are color-composite JPGs made from multi-band data. The exact process for creating the images depends on the bands and resolutions in the surveys.

For galaxies in the ACS-GC, color composites are made using a fixed pixel intensity scaling with weights of $[2.4 \times 10^{-4}, 3 \times 10^{-4}, 3 \times 10^{-4}]$ in the red, green, and blue channels respectively. A nonlinear mapping is applied to each pixel to emphasize the contrast in faint features (Lupton et al. 2004), taking the form of:

$$I_{\text{channel,new}} = I_{\text{channel,old}} \times \frac{\text{arcsinh}(b \times r)}{(b \times r)} \quad (1)$$

The GZH images from Griffith et al. (2012) use a value of $b = 3$.

The majority of the data in Legacy surveys described in §2.1 had images in only one or two filters available when the GZH project was first launched, making standard 3-channel RGB images in the same method used for the SDSS images in the original Galaxy Zoo impossible. For surveys with images in two bands (AEGIS, GEMS, and the two-epoch GOODS-N and GOODS-S), the lower-wavelength band was mapped to the blue channel, the higher-wavelength band to the red channel, and the green channel created by taking the geometric mean of the two. Bands used in each of the surveys are listed in Table 1. The 2-epoch GOODS-N and GOODS-

S images use different filters — this was a deliberate choice made so that the GEMS images could be directly compared with the overlapping coverage of GOODS-S (Figure 1).

By the time that the 5-epoch sets of GOODS data were put into GZH (in March 2015), coverage in four separate *HST* bands were publicly available. The deeper GOODS images were created using the arithmetic mean of B_{435W} and V_{606W} in the blue channel, I_{814W} in the red channel, and I_{850LP} in the green channel. These images also had the speckled noise pixels decolorized.

The COSMOS images only had the I_{814W} imaging available at the time of classification in GZH. For these galaxies, we created “pseudocolor” images by using the ACS I_{814W} data as the illumination map and ground-based imaging from the *Subaru* telescope in B_J , r^+ , and i^+ filters to provide the color gradients (see Griffith et al. 2012, for further details). This means that the images have the angular resolution of *HST* ($\sim 0.05''/\text{pixel}$) for the overall intensity, but the color gradients are at ground-based resolution, with seeing between $0.95''$ and $1.05''$ (Taniguchi et al. 2007).

The Stripe 82 single-epoch images were taken directly from the color composites on the DR7 SDSS Skyserver, which combines g' , r' , and i' exposures into the RGB channels. The coadded Stripe 82 images were assembled from runs 106 and 206 in DR7 and made into color composites using the method of Lupton et al. (2004).

To deal with images in which the sky noise was highly colored (which might have been a distraction to visual classification), a soft-edged object mask was applied that preserves the color balance for galaxies, but desaturates the speckled noise against regions of blank sky. This technique was applied only to the coadded Stripe 82 and the COSMOS images.

2.4. Images with simulated nuclear point sources

GZH also includes a set of images designed to measure the effect of active galactic nuclei (AGN) on morphological classifications. Since galactic nuclei can have bright, unresolved optical emission, this has the potential to mimic or distort the identification of a bulge component. The presence of an AGN is simulated by modeling the point spread function (PSF) of the telescope and then inserting a bright source near the center of a real galaxy. For each image, the simulated AGN is assigned one of three colors – either blue, red, or flat (white) as seen in the color images – and a range of brightnesses such that $L_{\text{ratio}} \equiv L_{\text{galaxy}}/L_{\text{AGN}}$ is in $(0.2, 1.0, 2.0, 5.0, 10.0, 50.0)$. Combining these parameters generates 15 images with

different simulated AGN for each host.

Two sets of simulated AGN were generated in GZH. The first set (version 1) was assembled from 95 galaxies from GEMS imaging and PSFs from `daophot`. The second set (version 2) was assembled from 96 galaxies in GOODS-S; this version used deeper imaging and improved PSFs from `TinyTim`.

Images with simulated AGN were classified in the main interface in an identical manner and evenly distributed with unaltered images of the galaxies. Classifiers were not explicitly told that the images had been altered, as the goal was to measure the effect on normal classifications in as unbiased a manner as possible.

2.5. Galaxy metadata

Photometric data for the bulk of the GZH sample is largely drawn from the tables provided in Griffith et al. (2012). This includes photometric parameters such as the fluxes, magnitudes, radii, ellipticities, position angles, and positions drawn from both SExtractor and GALFIT. GALFIT also provides the parametric Sérsic index and effective half-light radius for the best-fit model. All parameters are measured in both bands of the ACS imaging, with the exception of the single-band COSMOS images.

Redshifts for the GZH catalog are compiled from a variety of sources. For each galaxy, the primary redshift used for debiasing calculations (Section 4) is in the `Z_Best` column of Table 6. The redshift type (spectroscopic: `SPEC_Z`, photometric: `PHOTO_Z`, or grism: `GRISM_Z`) is listed in the column `Z_BEST_TYPE`, and the source catalog of the redshift is included as `Z_BEST_SOURCE`.

For galaxies which have published redshifts from multiple sources, the following algorithm is used to select the `Z_BEST` quantity. This first priority is spectroscopic redshifts; these are provided in the ACS-GC (Griffith et al. 2012), 3DHST (Momcheva et al. 2015), and MUSYC (Cardamone et al. 2010) catalogs. A high quality spectroscopic redshift in the ACS-GC is the primary option; if none is available, then `Z_BEST` uses the spectroscopic redshifts in 3DHST, and then MUSYC. For galaxies with multiple spectroscopic redshifts, more than 98% are consistent at $\Delta z < 0.001$, and so the order of selection makes no practical difference. If no spectroscopic redshifts are available, the $1-\sigma$ errors of the photometric (ACS-GC, 3DHST, MUSYC, UltraVISTA; Ilbert et al. 2013) and UltraVISTA grism data are used to select the redshift with the smallest error. Table 2 shows the results of this selection.

Table 2. GZH redshifts by survey

Survey	ACS-GC		3DHST		MUSYC		UltraVISTA		Total	
	spec-z	photo-z	spec-z	grism-z	photo-z	spec-z	photo-z	photo-z	with redshift	in survey
AEGIS	3,656	2,941	12	515	249	0	0	0	7,373	8,507
COSMOS	7,201	77,435	35	358	26	0	0	2,665	85,020	92,808
GEMS	387	628	6	99	40	279	7,304	0	8,743	9,304
GOODS-N	1,947	37	418	1,545	1,381	0	0	0	5,328	12,030
GOODS-S	1,080	4	327	1,348	281	816	1,184	0	5,040	10,284
SDSS	0	0	0	0	0	0	0	0	37,545	51,861
Total	14,271	81,045	798	3,865	1,977	1,095	8,488	2,665	114,204	184,794

Photometric and spectroscopic data for the SDSS Stripe 82 galaxies are taken from the CasJobs DR7 tables. This includes *ugriz* Petrosian magnitudes and fluxes, as well as the relative de Vaucouleurs and exponential fits from the model magnitudes. Redshifts used for the SDSS galaxies are all spectroscopic. 82.6% of galaxies in the single-depth images and 65.1% of galaxies in the coadd images have a measured DR7 spectroscopic redshift.

3. GALAXY ZOO INTERFACE AND CLASSIFICATIONS

3.1. User weighting

The votes of individual users who classified galaxies in GZH are combined to make a vote fraction for each question on the classification tree. Users' votes are weighted slightly (in a method identical to that described in Willett et al. 2013) such that users who frequently disagree with all other users end up having very low weights. The user weighting w is 1 for the top 95% of users as ranked by consistency. For the bottom 5% of users, w drops smoothly and is effectively zero for only the bottom 1% of classifiers in the CDF. The overall effect on the GZH dataset is relatively small, but this method is effective at filtering out contributions from random or deliberately malicious classifiers.

3.2. Interface and decision tree

Describe the GZ interface and the hierarchical decision tree.

4. CORRECTING FOR REDSHIFT-DEPENDENT CLASSIFICATION BIAS

The previous versions of Galaxy Zoo morphology classifications (Lintott et al. 2008; Willett et al. 2013) were based on observations of galaxies in the Sloan Digital Sky Survey (SDSS) which have a median redshift of $z < 0.2$. In these cases, it was assumed that there was no cosmological evolution of the morphologies of galaxies

and therefore any observed changes in the distribution of galaxies with different consensus morphologies was due to the effects of redshift on the image quality (*i.e.*.. the reduction in physical resolution, surface brightness dimming, etc). For both previous releases of GZ morphologies, a correction for redshift-dependent bias was applied based on matching the classification fractions at the highest redshfts with those at the lowest redshift. Bamford et al. (2009) and Willett et al. (2013) provide complete descriptions of the process for GZ1 and GZ2, respectively.

In the GZH samples, the redshift range is large enough that cosmological evolution of the types and morphologies of galaxies is expected for galaxies in the sample. As a result, the previous methods of correcting for redshift dependent bias will not work. In addition, the effects of band shifting will change the images even more across these redshift ranges.

In order to test and correct for the effects of redshift, GZH includes a set of calibration images. These images consist of the same galaxy as it would appear over a variety of redshifts. The input images are from the SDSS (York et al. 2000; Strauss et al. 2002) and are processed using the FERENGI code (Barden et al. 2008) to match the observational properties of the *HST* surveys out to $z = 1$. These images were classified in the Galaxy Zoo interface using the same classification scheme as the original *HST* images.

4.1. Selection of FERENGI input galaxies

The GZH classifications include 288 unique galaxies originally generated from SDSS imaging and processed with the FERENGI code. The selection spanned a variety of galaxy morphologies (as selected by GZ2 classifications) and r' -band surface brightnesses, and also spanned the redshift range of SDSS targets (in $N_z = 4$ bins) in order to be optimized for different target minimum redshifts in *HST* imaging.

The surface brightness selection ($N_\mu = 3$) for the FERENGI galaxies was (1) low: $\mu > 21.5 \text{ mag arcsec}^{-2}$;

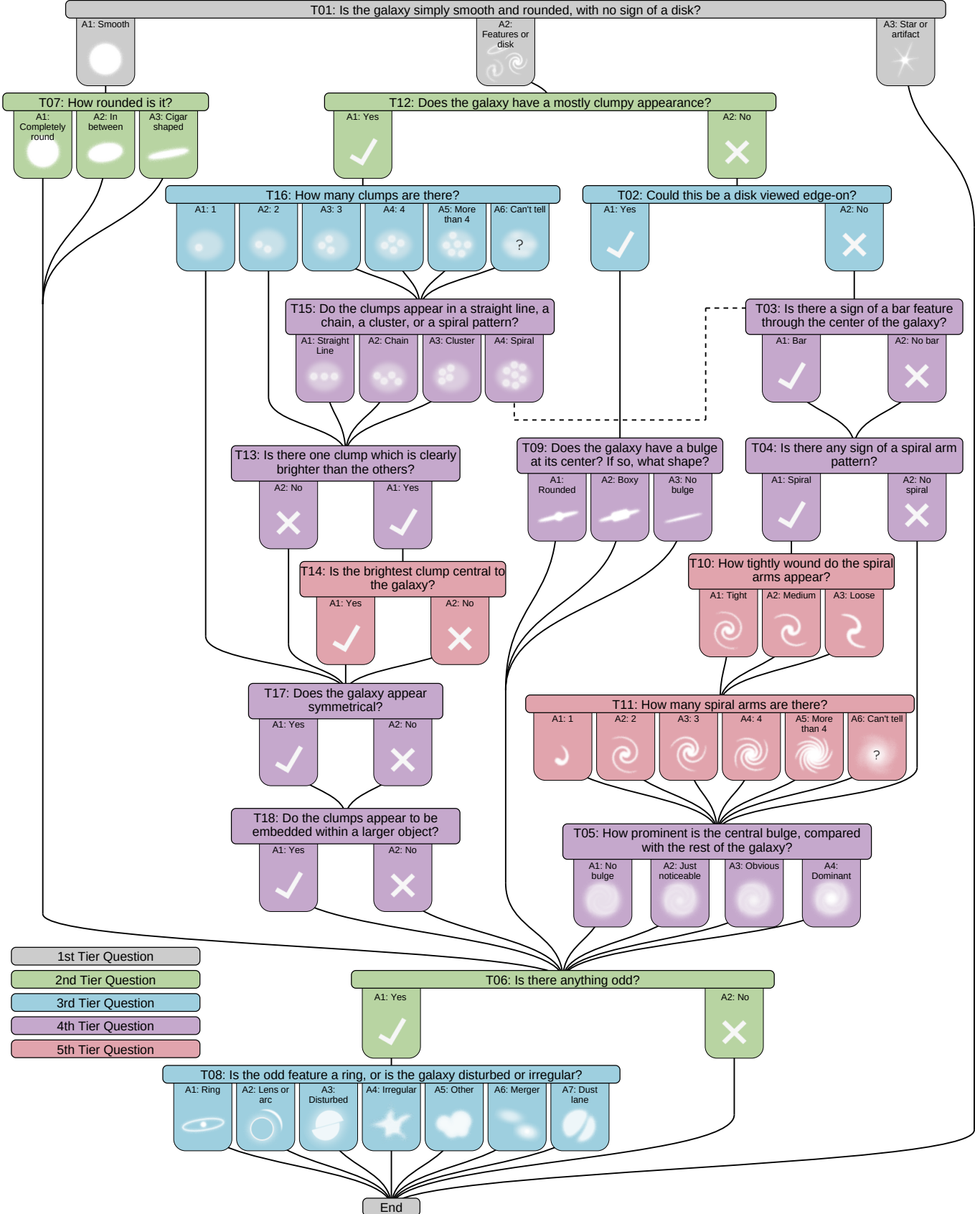


Figure 2. Flowchart of the questions presented to GZH users, labeled with the corresponding Task numbers. Tasks in the decision tree are color-coded by tier level: Gray-colored Tasks are 1st tier questions which are asked of all users. Tasks colored green, blue, purple, and pink (respectively) are one, two, three, or four steps below branching points in the decision tree.

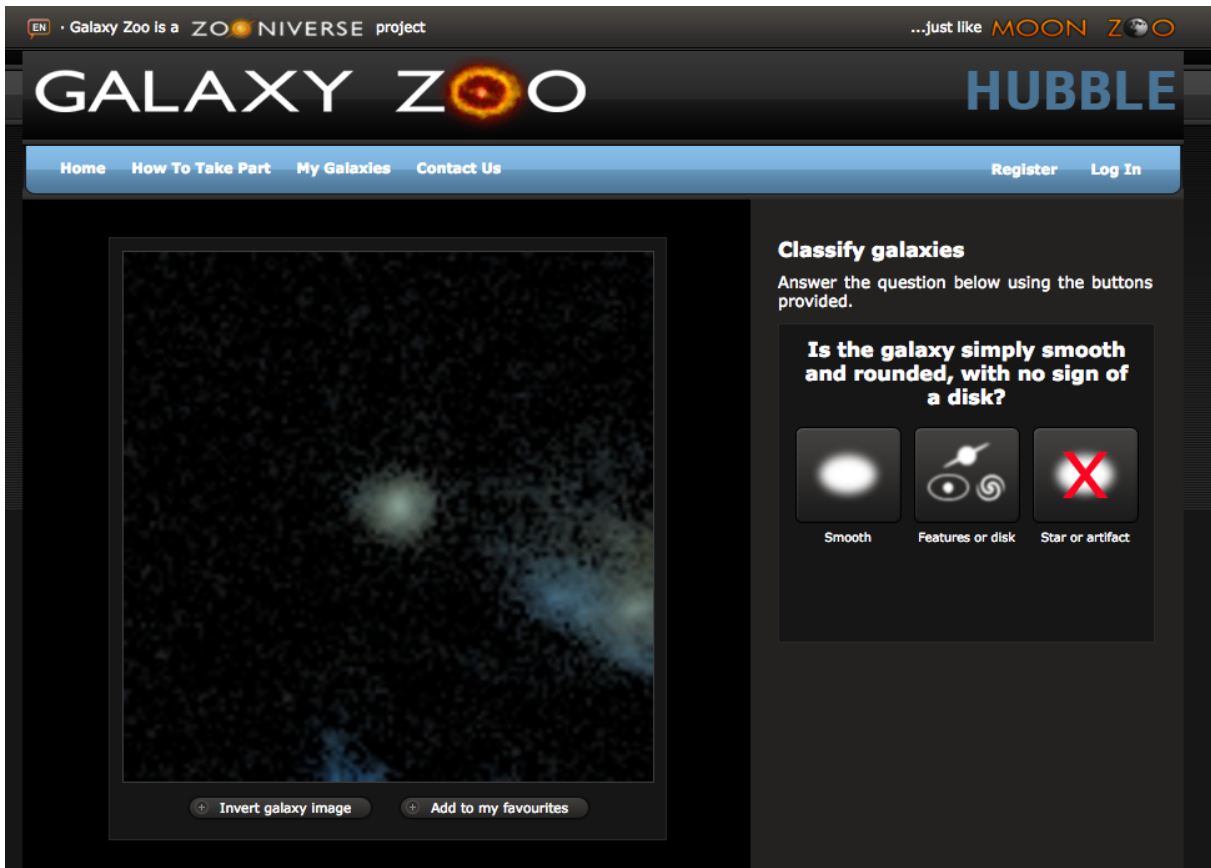


Figure 3. Screenshot of the Galaxy Zoo: Hubble interface at the beginning of a classification, with the user ready to select an answer for the first question in the decision tree.

Table 3. Summary of FERENGI artificial redshifting

z_{sim}	N_{zbins}	$N_{\text{evolution}}$	e_{max}	N_{galaxies}	N_{images}
0.3	8	7	-3.0	72	4032
0.5	6	4	-1.5	72	1728
0.8	3	3	-1.0	72	648
1.0	1	3	-1.0	72	216

(2) mid: $20.5 < \mu < 21.5 \text{ mag arcsec}^{-2}$; and (3) high: $\mu < 20.5 \text{ mag arcsec}^{-2}$. For each of the four “target redshifts” ($z_{\text{sim}} = 0.3, 0.5, 0.8$ and 1.0), the images were redshifted in $\Delta z = 0.1$ bins up to $z_{\text{sim}} = 1.0$.

In addition to the physical parameters of the input images, the FERENGI output depends on assumptions of the global galaxy evolution model. This evolution is a crude mechanism that mimics the brightness increase of galaxies with increasing redshift (out to at least $z \sim 1 - 2$). The effect on the redshifted images is simply an empirical addition to the magnitude of a galaxy of the form $M' = e \times z + M$, where M' is the corrected magnitude, and e is the evolutionary correction in magnitudes (i.e., $e = -1$ essentially brightens the galaxy by 1 magnitude by $z = 1$). FERENGI was run on the images for values of e starting from $e = 0$ and decreasing to $e = -3.5$ in increments of $\Delta e = 0.5$. Figure 4 shows several examples of the effects of “losing” spiral/disc features with increasing redshift for two galaxies with $e = 0$.

The final number of FERENGI images produced for each galaxy is ultimately a function of galaxy’s redshift, since the new images cannot be resampled at better angular resolution than the original SDSS data, as well as the number of e values selected. Table 3 summarizes the total sample of redshifted images produced for GZH.

4.2. Correcting GZH morphologies for classification bias

The approach used in GZH for correcting the weighted classifications for user bias rests on the assumption that the *amount* of bias is a function of the apparent size and brightness of the image as seen on screen. This is controlled by two types of parameters: **intrinsic** properties of the galaxy itself, such as its physical diameter and luminosity, and **extrinsic** properties, such as the distance (redshift) of the galaxy and its relative orientation. There are likely other parameters that affect user accuracy, such as the proximity of close companions (“distraction bias”; see Johnson et al. 2015) or bias as a function of the individual user. The combination of all such parameters forms a high-dimensional space, and there are insufficient data to measure their individual effects. Instead, this method uses only two parameters intended to capture the bulk of the change in bias (based on GZ1/GZ2): the r' -band surface brightness (μ_r ; intrinsic) and redshift (z ; extrinsic).

The change in bias as a function of μ_r and z_{sim} is measured using the FERENGI images over all the evolutionary correction factors. It is assumed that the “true” (ie, debiased) vote fraction $f_{\mu,z}$ for a galaxy can be expressed as:

$$f_{\mu,z} = (f_{\mu,z=0.3}) \times e^{\frac{z-z_0}{\zeta}}, \quad (2)$$

where $f_{\mu,z=0.3}$ is the “calibrated” vote fraction at the lowest redshift in the FERENGI bins ($z = 0.3$) and ζ is a positive parameter that controls the rate at which f decreases with increasing redshift. This formula fits the data relatively well (with almost no exceptions, the vote fractions for featured galaxies decrease monotonically with increasing redshift), and the exponential function bounds the observed vote fractions between $f_{\mu,z=0.3}$ and zero. Figure 5 show examples of the change in vote fraction and their fits to Equation 2 for a random selection of galaxies in the FERENGI images.

GZH uses the values of ζ for *all* sets of artificially redshifted galaxies to fit the overall distribution as a function of surface brightness, since the correction being applied is expected to vary as a function of the intrinsic galaxy properties. The galaxies that can be used to measure the calibration are restricted to those with a non-zero f_{features} at $z_{\text{sim}} = 0.3$ and with a reasonable fit ($\Delta\chi^2 > 3.0$) to the exponential model for the measured change in f_{features} .

Figure 6 shows the results of fitting the FERENGI images with Equation 2; the correction is a weak function of galaxy surface brightness. Higher-surface brightness galaxies have stronger average corrections, likely because these galaxies are more likely to have larger f_{features} values at high redshifts. Low surface brightness galaxies are more likely to begin low and remain low; the bounded nature of the dropoff (and Poissonian-like variance among the individual voters) means that the average magnitude of ζ will be less.

The data in Figure 6 are fit with a linear function such that:

$$\log_{10}(\hat{\zeta}) = \zeta_0 + (\zeta_1 \times \mu), \quad (3)$$

where $\hat{\zeta}$ is the correction factor applied to each galaxy as a function of surface brightness. The best-fit parameters to the linear fit (from least-squares optimization) are $\zeta_0 = 0.1$, $\zeta_1 = 1.4$. To make the final debiased correction, the simple exponential form of Equation 2 is modified to bound the debiased vote fractions between f and 1:

$$f_{\text{features,debiased}} = 1 - (1 - f)e^{\frac{z-z_0}{\hat{\zeta}}}. \quad (4)$$

4.3. Results of ζ approach

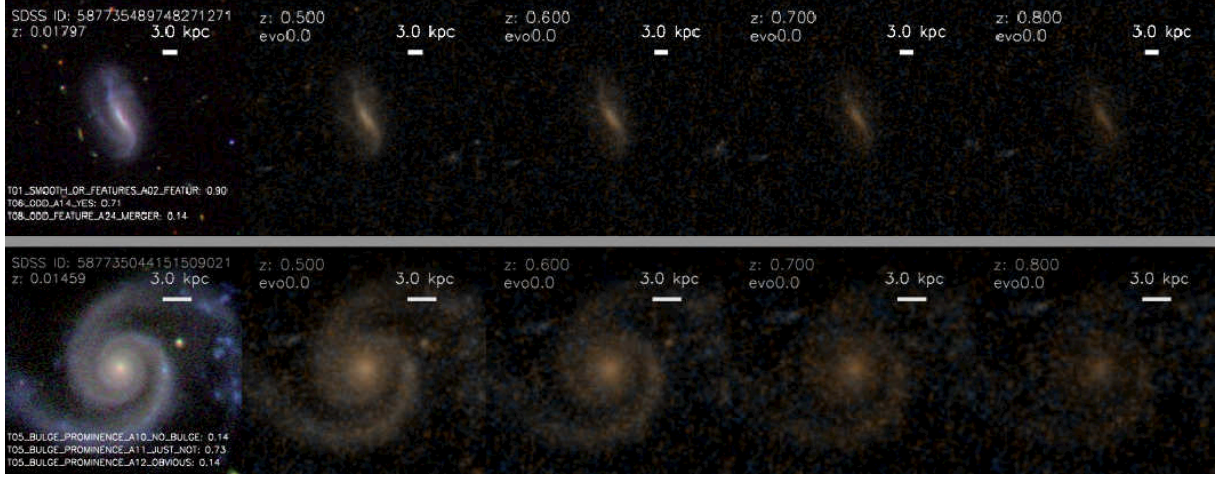


Figure 4. Examples of two galaxies which have been run through the FERENGI code to produce simulated *HST* images. The measured value of p_{features} from GZH for the images in each panel are (1) Top row: $p_{\text{features}} = (0.900, 0.625, 0.350, 0.350, 0.225)$ and (2) Bottom row: $p_{\text{features}} = (1.000, 0.875, 0.875, 0.625, 0.375)$.

Figure 8 shows the change in p_{features} for the FERENGI galaxies relative to their lowest simulated redshift. In this analysis, only galaxies whose lowest simulated redshift image was $z_{\text{sim}} = 0.3$ were used (see Table 3), and only those which had detectable surface brightness measurements in SExtractor; this includes 3,950 of the total 6,466 images. For each simulated redshift value z , and at a fixed surface brightness μ , $p_{\text{features},z}$, the value measured at that simulated redshift, is plotted against $p_{\text{features},z=0.3}$, the value measured for the same galaxy imaged at $z = 0.3$.

The objective is to use these data to predict, for a galaxy with a measured $p_{\text{features},z}$ value, what its p_{features} value *would have been* if it had been viewed at $z = 0.3$. This predicted value is defined as the debiased vote fraction $p_{\text{features,debiased}}$, and is calculated by applying a correction to the measured value of p_{features} , determined by the ζ function described in the previous section. A reliable predicted value can be obtained so long as the relationship between $p_{\text{features},z}$ and $p_{\text{features},z=0.3}$ is single-valued; that is, for a given $p_{\text{features},z}$, there is exactly one corresponding value of p_{features} at $z = 0.3$.

Figure 8 shows that the relationship between $p_{\text{features},z}$ and $p_{\text{features},z=0.3}$ is *not* always single valued; hence, it is not appropriate to correct galaxies that lie in certain regions of surface brightness/redshift/ p_{features} space. These regions tend to have low p_{features} values at high redshift, but a wide range of values at $z = 0.3$. These regions contain two morphological types of galaxies: the first set are genuine ellipticals, which have low values of p_{features} at both high and low redshift. The second group are disks whose features become indistinct at high redshift; hence their p_{features} value at $z = 0.3$ may be quite high, while the value observed at high redshift is very low. This effect is strongest at high z and low

μ , where features become nearly impossible to discern in the images.

The criteria for determining whether a region of this space is single-valued, and therefore correctable, is as follows: In each surface brightness and redshift bin, the relationship between $p_{\text{features},z}$ and $p_{\text{features},z=0.3}$ is modeled by fitting the data with a polynomial of degrees $n = 3, 2$, and 1 , and using the best fit out of the three. These fits are shown as the dashed black lines in Figure 8(a). Any flat regions of the polynomial fits are areas in which there is not a clear single-valued relationship between $p_{\text{features},z}$ and $p_{\text{features},z=0.3}$; this is quantified by setting a minimum slope cut of 0.4 . Any data in which the polynomial fit has a slope less than this value is considered *not* one-to-one, and therefore $p_{\text{features},z}$ cannot be boosted to its $p_{\text{features},z=0.3}$ value. Galaxies in this region are referred to as the *lower limit* sample. These regions are highlighted in blue in Figure 8(a). Uncolored (white) regions of the plot have sufficiently high slopes to consider the relationship as single-valued; galaxies in these regions are considered “correctable”, and only these are used in measuring the parameters for the ζ function (Section 4.2). Only surface brightness/redshift bins with at least 5 galaxies were considered; regions with fewer than 5 galaxies are considered to have “not enough information” to determine the $p_{\text{features},z}$ and $p_{\text{features},z=0.3}$ relationship, colored gray in Figure 8(a).

The unshaded regions in Figure 8(a) define discrete ranges of redshift, surface brightness, and p_{features} a galaxy must have in order for the debiased correction to be confidently applied to a galaxy in the GZH sample. While the appropriate correctable regions were defined discretely, the true correctable region is assumed to be a smooth function of z , μ , and p_{features} . To define this



Figure 5. Behavior of the normalized, weighted vote fractions of features visible in a galaxy (f_{features}) as a function of redshift in the artificial FERENGI images. Galaxies in this plot were randomly selected from a distribution with $e = 0$ and at least three detectable images in redshift bins of $z \geq 0.3$. Measured vote fractions (red points) are fit with an exponential function (Equation 2); the best-fit parameters are given above each plot. Error bars are Poissonian, assuming a median of 40 votes per galaxy.

smooth space, a convex hull is generated that encloses the correctable and lower-limit FERENGI galaxies in z - μ - p_{features} space. The boundaries are then adjusted until the contamination from both groups is minimized. The resulting hulls define the correctable and lower-limit regions for categorizing the *HST* galaxies. The results of this method and final categorization of the *HST* sample is displayed in Table 5. Of the galaxies at redshift higher than $z = 0.3$, 17% can be debiased using the ζ method, 27% cannot be debiased, and 56% cannot have the potential for a correction determined, due either a lack of redshift for the host galaxy or insufficient FERENGI images corresponding to the relevant z - μ values.

For the “lower-limit” galaxies for which a single debiased p_{features} value cannot be confidently assigned, the

range of debiased values is estimated using a method visualized in Figure 8(c). This uses the FERENGI simulated data to analyze the range of intrinsic $p_{\text{features}, z=0.3}$ values for any given observed p_{features} value, again as a function of surface brightness and redshift. Each z - μ bin, shows the spread of intrinsic values of $p_{\text{features}, z=0.3}$ for four ranges of observed p_{features} . The range of intrinsic values is defined as the inner 80% of the data, represented by the orange bars in Figure 8(c). For any galaxy which cannot be directly debiased by the ζ method, these ranges are used to denote the upper and lower limits on the expected values $p_{\text{features}, z=0.3}$ as a function of the observed p_{features} .

Few galaxies in the sample have sufficiently high corrections to completely change them from being confi-

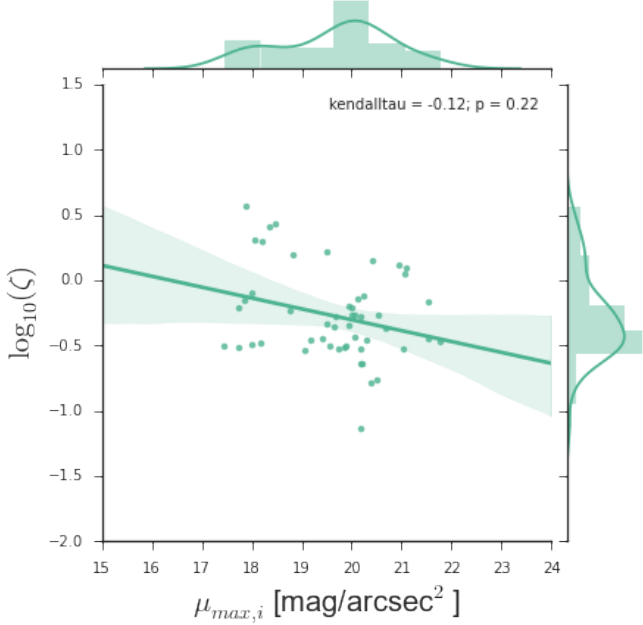


Figure 6. All fits for the vote fraction dropoff parameter ζ for f_{features} in the FERENGI galaxies as a function of surface brightness. This includes only the 37 galaxies with a reasonably bounded range on the dropoff ($-10 < \log(\zeta) < 10$) and sufficient points to fit the function.

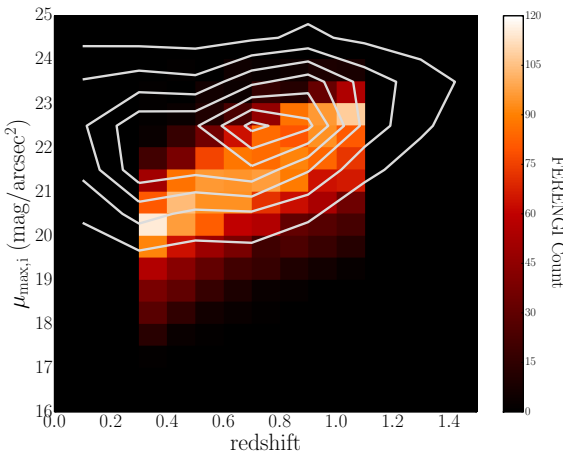


Figure 7. Surface brightness as a function of redshift for 3,950 FERENGI images and the 102,548 galaxies in the ACS sample with measured μ and z values. The color histogram shows the number of FERENGI images as a function of μ and z_{sim} . White contours show counts for the full ACS sample, with contours starting at $N = 1000$ and separated by intervals of 1000 up to 7000.

dently smooth to featured following the bias correction (Figure ??). As a check, highly boosted galaxies are compared to the expert classifications in the CANDELS catalog (Kartaltepe et al. 2015). There are only eight galaxies that were strongly boosted ($p_{\text{features,raw}} < 0.2$

Table 4. Distribution of FERENGI images analysed in Figure 8. Correctable images have a single-valued relationship between their measured p_{features} values at high and low redshifts (white regions in Figure 8). Images with only a lower-limit on p_{features} have a non single-valued relationship (blue regions). NEI images have undetermined relationships due to a lack of data ($N < 5$) in their corresponding z - μ bins (gray regions).

	N	%
Correctable	1,884	48%
Lower-limit	1,986	50%
NEI	80	2%
Total	3,950	100%

and $p_{\text{features,best}} > 0.5$) in GZH and also appears in the CANDELS expert sample. Of those eight galaxies, Kartaltepe et al. (2015) classifies 5 as spheroids, 2 as disks, and 1 as irregular/disky. The $p_{\text{features,best}}$ values for GZH are all between 0.5 and 0.6, making them intermediate disk candidates. One of the spheroids has hints of an interaction or minor merger to the south that may have been missed by the CANDELS experts, but almost all images are dim and with very low surface brightnesses in the ACS imaging, making positive identification challenging. Since the surveys use different rest-frame filters and the overlap sample is tiny, though, detailed comparisons between the overall morphologies are highly difficult.

4.4. Challenges of debiasing questions beyond “smooth or features”

As with the HST images, each FERENGI subject has a varying number of users answering the various questions in the hierarchical decision tree. Every user answers the first question, “Is the galaxy smooth and rounded, with no sign of a disk?”; as such the vote fractions p_{smooth} , p_{features} , and p_{artifact} are all computed with the minimum statistical error for any question, with roughly 40 total answers (see Section 3). The number of users to answer any subsequent question, however, is always equal to or less than the number to answer the preceding question. The average number of responses per task for fourth- or fifth-tier questions such as spiral arm structure (Tasks 12–14) is only 4 ± 4 for the FERENGI sample; while this distribution is strongly bimodal (reflecting the true morphologies of selected galaxies), the very low absolute numbers of votes introduce very high variance when attempting to calculate a statistical correction.

In the FERENGI data, these numbers severely limit the amount of information that can be extracted for the higher-tier questions. The debiasing technique used (Section 4.2) requires that at least 10 users answer each question for a galaxy with $z_{\text{sim}} = 0.3$ and the corre-

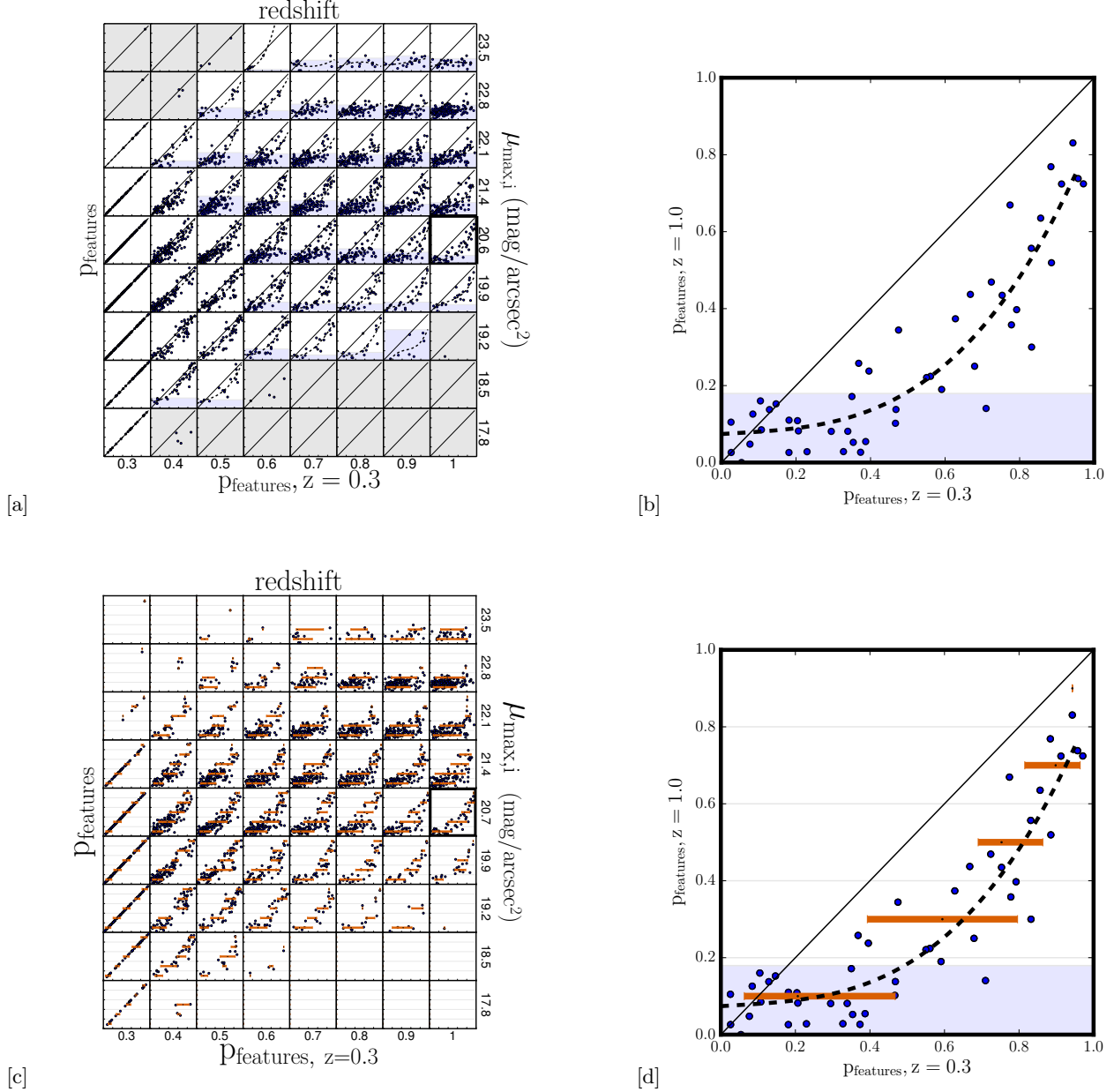


Figure 8. Effects of redshift bias in 3,950 images in the FERENGI sample. [a]: Each point in a given redshift and surface brightness bin represents a unique galaxy. On the y -axis in each bin is the p_{features} value of the image of that galaxy redshifted to the value corresponding to that redshift bin. On the x -axis is the p_{features} value of the image of the same galaxy redshifted to $z = 0.3$. The dashed black lines represent the best-fit polynomials to the data in each square. The solid black line represents $p_{\text{features},z} = p_{\text{features},z=0.3}$. Regions in which there is a single-valued relationship between p_{features} at high redshift and at $z = 0.3$ are white; those in which there is not are blue, and those with not enough data ($N < 5$) are gray. [b]: A larger version of the dark-outlined square in [a], containing FERENGI galaxies that have been artificially redshifted to $z = 1.0$ and have surface brightnesses between $20.3 < \mu < 21.0$ (mag/arcsec 2). [c]: The same data as [a] is shown. Each z, μ bin is divided into 4 sub-bins to determine the range of intrinsic $p_{\text{features},z=0.3}$ for a given range of observed $p_{\text{features},z}$ values. In each sub-bin, the orange bars represent the inner 80th percentiles of the data, the boundaries of which are the lower and upper limits of the debiased values. [d]: The same data as [b], but highlighting the upper and lower limit regions.

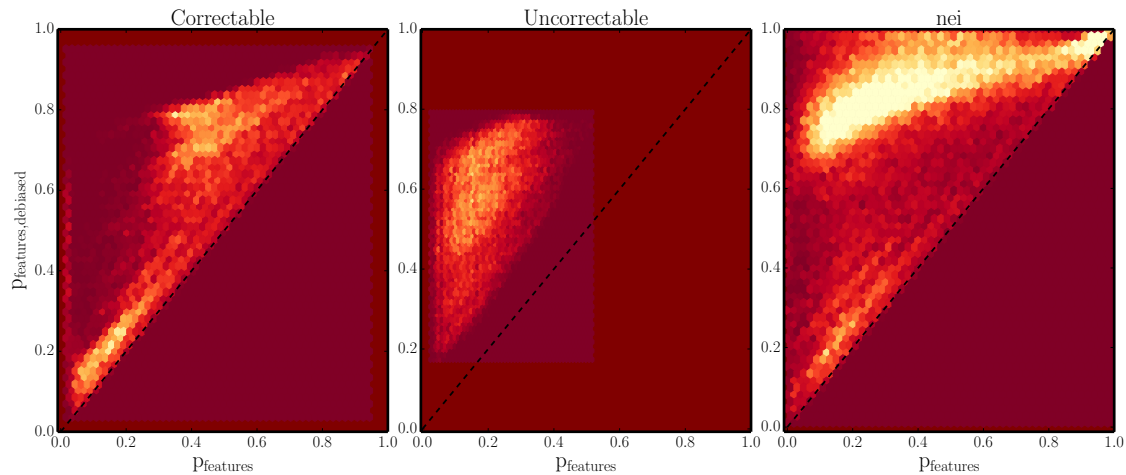


Figure 9. Debiased $p_{features}$ corrected to $z = 0.3$ vs weighted $p_{features}$ for the correctable (left), lower-limit (middle), and NEI (right) galaxies in the GZH sample.

sponding image at higher redshift. This requirement is (by default) met by all galaxies for the smooth/features question. However, this is often *not* met for questions beyond Task 01; on average, $60\% \pm 24\%$ of the galaxies do not have sufficient data to measure a correction, as compared to 2.0% achieved for Task 01 (Table 4). Of the remaining FERENGI galaxies which did meet this requirement, polynomials were fit to the data in each redshift-surface brightness bin, as was done for Task 01. The goodness-of-fit was evaluated in each bin, for each Task, using a normalized χ^2 metric. The mean χ^2 for all higher-order tasks was 0.10 ± 0.04 , significantly larger than the Task 01 value of 0.04. Based on this statistic, the data cannot not be modeled with sufficient confidence for the higher order tasks. An example of the debiasing technique applied to p_{bar} is shown in Section A.2; visual inspection of Figure A5 confirms that the points in each bin are scattered to a degree at which no strong correlation is present. For these reasons, debiased vote fractions are only offered in the GZH catalog for Task 01 (smooth/features).

5. THE GZH CATALOG

The data release for GZH includes morphological data for 181,101 images (generated from a total of 150,771 unique galaxies). The full table can be accessed at <http://data.galaxyzoo.org>. The online data also includes a secondary metadata table, which is drawn from a variety of sources detailed in Section 2.

Each image is listed under a unique project ID (eg, AHZ000001); the actual galaxy in the image is identified by the combination of the OBJNO and original survey. For each of the 55 responses in the GZH decision tree, the following classification data is provided: for each question, N_{votes} is the number of users to answer that question. For each unique answer, **fraction** is the fraction of users to select that answer ($N_{\text{answer}}/N_{\text{votes}}$), and **weighted** is the weighted fraction, which takes into account user consistency (Section 3.1).

The GZH vote fractions can be largely dependent on the resolution of the image. Two otherwise morphologically identical galaxies which differ significantly in redshift, brightness, or size may result in very different vote fractions for any given question, given that many features of a galaxy are difficult to discern in less-resolved images (bars, spiral arms, disk structure, etc). For this reason, it is necessary to take caution utilizing vote fractions as cut-offs to determine morphological structure; guidelines for careful classification are given in Section 6.

The GZH catalog is corrected for classification bias

only for the first question of the GZH decision tree (Section 4), which asks “*Is the galaxy smooth and round, with no sign of a disk?*” For this question, the catalog provides the additional parameters **debiased**, **lower limit**, **upper limit**, and **best** vote fractions. The **best** fraction for p_{features} is chosen based on the categorization of the galaxy: if it is “correctable”, **best** = **debiased**, if a lower limit, **best** = **lower limit**, and if neither, **best** = **weighted**.

The debiased and best vote fractions for p_{smooth} were calculated on the criteria that vote fractions for all answers must sum to unity, such that:

$$p_{\text{smooth}} \equiv 1 - p_{\text{features,best}} - p_{\text{artifact}}. \quad (5)$$

In rare cases (< 1% of the sample), this requirement resulted in negative vote fractions for p_{smooth} ; these were cases in which the p_{features} vote fraction was boosted to a high value relative to the p_{artifact} vote fraction. In these cases, the constraint that the vote fractions must sum to 1 is met by setting $p_{\text{smooth}} = 0.0$ and decreasing p_{features} accordingly. This correction is typically small, with a median decrease/increase of $p_{\text{features}}/p_{\text{smooth}}$ of $\Delta p = 0.04$.

Data products for GZH are split by the type of image being classified. Table 6 contains the classifications for the *HST* images from the AEGIS, COSMOS, and GEMS surveys, as well as 5-epoch deep imaging from the GOODS-N and GOODS-S surveys. This contains 118,425 galaxies and is the primary output from the GZH project. The next two tables have data for a small subset of 3,927 COSMOS images that were reprocessed to study the effect of color balance on morphological classification. Table 7 has images that are desaturated to minimize the color contrast; Table 8 has images with the red and blue color channels inverted. Table 9 contains data for 6,144 galaxies with 2-epoch images from GOODS. These have been mostly supplanted in the main table with deeper 5-epoch GOODS imaging; however, there are 1,683 galaxies in the shallower imaging that were not classified in the deeper mosaics. This data can also be compared to the counterparts in Table 6 to study the effect of depth on morphological classification. Tables 10 and 11 contain data for the SDSS Stripe 82 single-depth and co-added images, respectively, that were classified using the GZH interface and decision tree. Finally, Table 12 contains classifications for images with artificial point sources intended to simulate the effect of a bright AGN, as used in Simmons et al. (2014).

Table 5. Correctable fractions for the top-level task in GZH, split by survey.

	Correction type	AEGIS	COSMOS	GEMS	GOODS-N	GOODS-S	SDSS	Total
Correctable	0	1,654	15,170	1,837	993	835	0	20,489
Lower-limit	1	1,917	26,113	2,423	1,385	1,282	0	33,120
No Correction Needed ($z \leq 0.3$)	2	955	11,926	1,175	415	400	37,545	52,416
NEI	3	2,847	34,511	3,308	2,535	2,523	0	45,724
No Redshift Information	4	1,134	5,088	561	687	102	14,316	21,888
Total		8,507	92,808	9,304	6,015	5,142	51,861	173,637

Table 6. GZH morphological classifications for *HST* images from AEGIS, COSMOS, GEMS, and GOODS

Project ID	Hubble ID	Imaging	t01_smooth_or_features_			t01_smooth_or_features_a01_smooth_					...
			Correction ¹	N_votes	fraction	weighted	debiased	best	lower limit	upper limit	
AHZ100002g	10010842	AEGIS	0	127	0.118	0.128	0.085	0.085	0.226	0.226	
AHZ100002h	10010870	AEGIS	4	127	0.567	0.592	0.927	0.592	—	—	
...											
AHZ20004kd	20014731	COSMOS	3	44	0.682	0.675	0.147	0.675	—	—	
AHZ20004ke	20014732	COSMOS	2	45	0.689	0.756	0.893	0.756	—	—	
...											
AHZ400043g	90022729	GEMS	1	121	0.702	0.733	0.487	0.734	0.483	0.800	
AHZ4000416	90022735	GEMS	1	127	0.646	0.698	0.508	0.698	0.171	0.727	
...											
AGZ0007z47	10014	GOODS-N-FULLDEPTH	1	40	0.475	0.475	0.197	0.475	0.011	0.496	
AGZ0007z48	10017	GOODS-N-FULLDEPTH	3	40	0.675	0.675	0.048	0.675	0.168	0.669	
...											
AGZ00083jb	8869	GOODS-S-FULLDEPTH	1	40	0.425	0.425	0.109	0.425	0.070	0.548	
AGZ00083jc	8878	GOODS-S-FULLDEPTH	0	40	0.205	0.205	0.048	0.048	-0.005	0.287	
...											

¹ Flag indicating how the vote fractions for this galaxy were corrected through debiasing (§4.3), if possible. 0 = correctable, 1 = lower-limit ($p_{\text{raw}} - p_{\text{adj}}$ is not single-valued), 2 = uncorrected ($z_{\text{gal}} < 0.3$), 3 = uncorrected (insufficient FERENGI galaxies in this $z-\mu$ bin), 4 = uncorrected (no galaxy redshift available).

NOTE—The full version of this table is available in electronic form, as well as at <http://data.galaxyzoo.org>. The complete version includes data for 118,425 galaxies and morphological information for all tasks in the tree. A subset of the information is shown here to illustrate form and content.

Table 7. GZH morphological classifications for color-faded Hubble images

Project ID	Hubble ID	Imaging	t01_smooth_or_features_			t01_smooth_or_features_a01_smooth_					...
			Correction	N_votes	fraction	weighted	debiased	best	lower limit	upper limit	
AHZF000001	20000002	COSMOS	1	48	0.708	0.755	0.228	0.754	0.325	0.829	
AHZF000003	20000004	COSMOS	3	49	0.367	0.379	0.100	0.379	0.198	0.198	
AHZF000004	20000006	COSMOS	3	49	0.265	0.271	0.010	0.270	—	—	
AHZF00000z	20000102	COSMOS	1	44	0.727	0.78	0.233	0.780	0.316	0.820	
AHZF000010	20000104	COSMOS	2	53	0.811	0.849	0.904	0.848	—	—	
...											

NOTE—The full version of this table is available in electronic form, as well as at <http://data.galaxyzoo.org>. The complete version includes data for 3,927 galaxies and morphological information for all tasks in the tree. A subset of the information is shown here to illustrate form and content.

Table 8. GZH morphological classifications for color-inverted Hubble images

Project ID	Hubble ID	Imaging	t01_smooth_or_features_			t01_smooth_or_features_a01_smooth_				...
			Correction	N _{votes}	fraction	weighted	debiased	best	lower limit	
AHZC000001	20000002	COSMOS	1	168	0.615	0.664	0.160	0.663	0.271	0.775
AHZC000003	20000004	COSMOS	0	235	0.333	0.364	0.002	0.002	0.063	0.063
AHZC000004	20000006	COSMOS	3	316	0.235	0.252	-0.011	0.252	-	-
AHZC00000z	20000102	COSMOS	1	207	0.755	0.757	0.272	0.756	0.249	0.796
AHZC000010	20000104	COSMOS	2	158	0.843	0.882	0.936	0.881	-	-
...										

NOTE—The full version of this table is available in electronic form, as well as at <http://data.galaxyzoo.org>. The complete version includes data for 3,927 galaxies and morphological information for all tasks in the tree. A subset of the information is shown here to illustrate form and content.

Table 9. GZH morphological classifications for GOODS 2-epoch images

Project ID	Hubble ID	Imaging	t01_smooth_or_features_			t01_smooth_or_features_a01_smooth_				...
			Correction	N _{votes}	fraction	weighted	debiased	best	lower limit	
AHZ3000001	50000000	GOODS-N	0	123	0.390	0.415	0.090	0.090	-	-
AHZ3000002	50000001	GOODS-N	2	126	0.341	0.355	0.356	0.356	0.220	0.279
AHZ3000003	50000005	GOODS-N	1	129	0.760	0.826	0.633	0.825	0.596	0.834
AHZ3000004	50000008	GOODS-N	1	120	0.758	0.787	0.639	0.787	0.658	0.834
AHZ3000005	50000010	GOODS-N	1	123	0.854	0.890	0.611	0.889	0.597	0.914
...										

NOTE—The full version of this table is available in electronic form, as well as at <http://data.galaxyzoo.org>. The complete version includes data for 6,144 galaxies and morphological information for all tasks in the tree. A subset of the information is shown here to illustrate form and content.

Table 10. GZH morphological classifications for SDSS Stripe 82 single-epoch images

Project ID	SDSS DR7 ObjID	Imaging	t01_smooth_or_features_			t01_smooth_or_features_a01_smooth_				...
			Correction	N _{votes}	fraction	weighted	debiased	best	lower limit	
AHZ5000001	587730845812064684	SDSS	2	41	0.585	0.595	0.759	0.594	-	
AHZ5000002	587730845812065247	SDSS	2	46	0.609	0.651	0.897	0.651	-	
AHZ5000003	587730845812196092	SDSS	2	51	0.039	0.044	0.067	0.043	-	
AHZ5000004	587730845812196825	SDSS	2	35	0.514	0.605	0.928	0.605	-	
AHZ5000005	587730845812524122	SDSS	2	47	0.766	0.812	1.038	0.810	-	
AHZ5000006	587730845812654984	SDSS	2	42	0.5	0.542	0.680	0.541	-	
AHZ5000007	587730845812655541	SDSS	2	41	0.488	0.526	0.697	0.525	-	
AHZ5000008	587730845812720365	SDSS	2	53	0.792	0.84	1.050	0.839	-	
AHZ5000009	587730845812720640	SDSS	4	43	0.0	0.0	0.0	0.0	-	
AHZ500000a	587730845812720699	SDSS	2	40	0.425	0.478	0.588	0.477	-	
...										

NOTE—The full version of this table is available in electronic form, as well as at <http://data.galaxyzoo.org>. The complete version includes data for 21,522 galaxies and morphological information for all tasks in the tree. A subset of the information is shown here to illustrate form and content.

Table 11. GZH morphological classifications for SDSS Stripe 82 coadded images

Project ID	SDSS DR7 ObjID	Imaging	t01_smooth_or_features_		t01_smooth_or_features_a01_smooth_			...
			Correction	N _{votes}	fraction	weighted	debiased	
AHZ6000001	8647474690312306978	SDSS	4	40	0.275	0.289	0.762	0.289
AHZ6000002	8647474690312307154	SDSS	2	43	0.605	0.634	0.858	0.635
AHZ6000003	8647474690312307877	SDSS	2	51	0.608	0.627	0.906	0.627
AHZ6000004	8647474690312308301	SDSS	4	52	0.038	0.038	0.723	0.038
AHZ6000005	8647474690312308318	SDSS	2	44	0.614	0.632	0.776	0.631
AHZ6000006	8647474690312308880	SDSS	2	36	0.667	0.683	0.901	0.683
AHZ6000007	8647474690312372644	SDSS	4	48	0.646	0.674	1.145	0.674
AHZ6000008	8647474690312372789	SDSS	4	45	0.489	0.571	0.964	0.570
AHZ6000009	8647474690312372931	SDSS	4	47	0.553	0.587	0.926	0.587
AHZ600000a	8647474690312373190	SDSS	4	47	0.574	0.559	1.008	0.559
...								

NOTE—The full version of this table is available in electronic form, as well as at <http://data.galaxyzoo.org>. The complete version includes data for 30,339 galaxies and morphological information for all tasks in the tree. A subset of the information is shown here to illustrate form and content.

Table 12. GZH morphological classifications for *HST* images with simulated AGN

Project ID	SDSS DR7 ObjID	Imaging	Correction	Version	L _{ratio}	AGN color ¹	N _{votes}	t01_smooth_or_features_a01_smooth_			
								fraction	weighted	debiased	best
AHZ7000001	90024700	GEMS	1	1	0.2	1	42	0.238	0.239	-0.110	0.238
AHZ7000002	90024700	GEMS	1	1	1.0	1	51	0.255	0.265	-0.107	0.264
AHZ7000003	90024700	GEMS	0	1	5.0	1	47	0.170	0.167	-0.018	-0.018
AHZ7000004	90024700	GEMS	0	1	10.0	1	41	0.195	0.195	0.045	0.045
AHZ7000005	90024700	GEMS	0	1	50.0	1	47	0.170	0.178	0.067	0.067
...											
AHZ700013m	90024700	GEMS	0	2	0.0	0	35	0.171	0.136	0.011	0.011
AHZ700013n	90024700	GEMS	1	2	0.2	1	20	0.150	0.158	-0.278	0.049
AHZ700013o	90024700	GEMS	1	2	1.0	1	32	0.281	0.300	-0.086	0.281
AHZ700013p	90024700	GEMS	0	2	5.0	1	29	0.103	0.115	-0.098	-0.098
AHZ700013q	90024700	GEMS	0	2	10.0	1	35	0.171	0.181	0.027	0.027
AHZ700013r	90024700	GEMS	0	2	50.0	1	34	0.206	0.206	-0.005	-0.005
...											

¹ Flag indicating the color of the PSF in the simulated AGN. 0 = no simulated AGN, 1 = blue, 2 = flat, 3 = red.

NOTE—The full version of this table is available in electronic form, as well as at <http://data.galaxyzoo.org>. The complete version includes data for 2,961 galaxies and morphological information for all tasks in the tree. A subset of the information is shown here to illustrate form and content.

6. USING THE CATALOG

The intended purpose of the GZH catalog is to provide a simple, yet flexible, means of identifying samples of galaxies with a desired morphological type. This section provides instructions for creating such samples using the vote fractions corresponding to the tasks shown in Figure 2. We stress that the selection process will vary based on the particular science case. More conser-

vative cuts can be applied to create pure, but not necessarily complete, samples. These are useful for selecting galaxies exhibiting unique morphologies for individual case studies or observing proposals. Looser cuts can be applied to obtain samples with a higher level of completeness, which will increase the sample size but can potentially decrease purity. Population studies would make use of such large samples, in which statistical sig-

nificance is a crucial factor in evaluating results. [Masters et al. \(2011\)](#); [Melvin et al. \(2014\)](#); [Cheung et al. \(2015\)](#), and [Galloway et al. \(2015\)](#) are examples of GZ papers which select morphologies in this way.

In GZH, volunteers answer questions about a galaxy’s morphology in a decision tree format. With this structure, questions shown to a user are dependent on their answers to the previous questions. For example, a user is only asked Task 11, “*How many spiral arms?*” if they had answered “yes” to Task 10, which asks whether any spiral arms are present. This structure is used to reduce the workload of the users by only asking questions relevant to the particular galaxy; in this example, it would not be useful, nor would it make physical sense, to ask a user how many spiral arms in a galaxy which they had declared had no spiral arms to begin with. Figure 2 shows the possible paths available for answering the questions offered in GZH. The colors represent the tier level of Tasks, which indicate the number of previous Tasks the given Task is dependent upon. The arm-number question, Task 11, is a 5th tier Task, meaning that whether this question is seen by a user is dependent on four Tasks preceding it. In this case, it is only shown to volunteers who voted the galaxy was featured/disk-shaped in Task 01, not clumpy in Task 12, not edge-on in Task 02, and had spiral structure in Task 10.

To select galaxies of a morphological type identified with a particular Task, a cut is placed on the vote fraction for that Task (p_{task}), as well as the vote fractions for the Tasks preceding it, because of the dependency induced by the decision-tree structure. For example, to select barred galaxies, a cut may be placed on p_{bar} such that only galaxies where a high fraction of votes for this task voted for the *bar, yes* answer. This is not the only necessary cut, however, since not all users answer this question; only those who have previously selected “features” in Task 01, “not clumpy” in Task 12, and “not edge-on” in Task 02 will have the opportunity to vote on the bar question, Task 03. To ensure that p_{bar} is well-sampled, cuts on all previous tasks must be applied.

The flexibility of this catalog allows the user to set their own selection criteria for vote fraction thresholds to create a morphologically-pure sample. Table 13 provides baseline cuts for selecting galaxies of a variety of morphologies. These thresholds are determined by a visual inspection of subsamples. For each Task, at least 20 users are required to have voted on the given question along with a cut on the vote fraction is applied to the previous task. We visually analyzed subsamples of 50 galaxies meeting both criteria, as well as a control sample of galaxies which had 20 users vote on the task, but did not meet the threshold cut set for the previous task. The threshold cut was adjusted and new subsamples were inspected until both the original and control

samples achieved > 80% purity.

As an example of how to use Table 13 to create a sample of 3-armed spirals galaxies, one should select objects with $N_{\text{arm number}} \geq 20$, $p_{\text{features}} > 0.23$, $p_{\text{clumpy,no}} > 0.30$, $p_{\text{edgeon,no}} > 0.25$, and $p_{\text{spiral,yes}} > 0.25$. These cuts define a sample of galaxies of “arm number candidates”; ie galaxies for which answering the arm number question makes physical sense and the vote fraction $p_{\text{arm number}}$ is well-sampled. In this example, such galaxies are featured, non-clumpy, non-edge on, spiral galaxies. At this point a cut can be made on $p_{\text{arm number}}=3$ to select spirals with three arms.

Tasks 03, 04 and 05 have an additional possible pathway; as shown in Figure 2, a user might also be shown this question if they select “featured/disk” in Task 01, “clumpy” in Task 12, two or more clumps in Task 16, and “spiral arrangement” in Task 15. After applying the appropriate thresholds for this path, < 0.5% of the galaxies which have ≥ 20 answers to these questions used this pathway to arrive at these Tasks. Further, of these subjects, none were found to exhibit disk structure, although the clumps within were arranged in a spiral pattern.

This section described how to use the previous Task thresholds in Table 13 to select well-sampled galaxies which may or may not contain the feature associated with a unique Task. The following two examples show to use the vote fractions for a particular Task to obtain a sample of galaxies with a certain morphological type.

6.1. Example 1: Selecting bars

A sample of barred disk galaxies is created by applying cuts on the previous tasks as listed in Table 13. 11,049 “bar candidates”, galaxies for which asking the bar question is meaningful, were selected by applying the cuts $N_{\text{bar}} \geq 20$, $p_{\text{features}} > 0.23$, $p_{\text{clumpy,no}} > 0.30$, and $p_{\text{edgeon,no}} > 0.25$. These galaxies are featured, non-clumpy, non-edge on galaxies. Of these, a pure sample of 730 barred disks was identified by applying a cut of $p_{\text{bar}} > 0.7$. A subsample of 50 galaxies were visually inspected and 94% were found to contain strong bars. A complete sample of strong and weak bars was created by applying a cut of $p_{\text{bar}} > 0.3$. This sample contained 3,218 galaxies, 86% of which were found to contain weak or strong bars through visual inspection in a subsample of 50.

The resulting bar sample can be used to estimate the redshift evolution of bar fraction and find a steady decrease of $f_{\text{bar}} \sim 0.32$ at $z = 0.4$ to $f_{\text{bar}} \sim 0.24$ at $z = 1.0$. The decrease in bar fraction agrees with [Melvin et al. \(2014\)](#), although they report a lower overall bar fraction going from $f_{\text{bar}} = 0.22$ at $z = 0.4$ to $f_{\text{bar}} = 0.11$ at $z = 1.0$. The difference in total bar fraction is expected, as this analysis used a looser cut on p_{bar} , there is no lu-

minosity cut, and the use of debiased values for p_{features} increases the total amount of disks in the sample compared to Melvin et al. (2014). For a more thorough analysis of the bar fraction, a cut on p_{bar} that evolves with redshift may yield more accurate results, since there are no explicit debiased values of p_{bar} that would take redshift induced bias into account.

6.2. Example 2: Identifying clump multiplicity

Clumps are known to be a characteristic feature of galaxies outside the local universe, and there is evidence they play a crucial role in the evolution of modern spirals, particularly in the formation of central bulges (Elmegreen et al. 2005; Elmegreen & Elmegreen 2014; Guo et al. 2015; Behrendt et al. 2016). Simulations show clumps migrate from the outer disk to the galactic center on relatively short (a few orbital periods) timescales (Mandelker et al. 2015) and observations show increasing bulge to clump mass and density ratios as the universe evolves since $z \sim 1.5$ (Elmegreen et al. 2009), suggesting that clumps coalesce over time to form the modern bulges of disk galaxies. GZH added a “clumpy” path to the decision tree for the purpose of both identifying clumps and investigating their evolution with redshift.

For galaxies identified as “clumpy” in GZH, the number of clumps can be determined using Task 16. Table 13 can be used to select 8,444 galaxies measured as “clumpy” using $p_{\text{features}} > 0.23$ and $p_{\text{clumpy},\text{yes}} > 0.80$ to ensure the vote fractions for Task 16 are well-sampled. The clump number can be reasonably identified for 1,112 of the clumpy galaxies; for the remainder, the unique clumps were less distinguishable from each other and the exact number of clumps could not be deduced without careful visual inspection. In the 1,112 which did have distinguishable clumps, there are 61 one-clump galaxies using $p_1 \text{ clump} > 0.50$, 442 two-clump galaxies using $p_2 \text{ clumps} > 0.80$, 275 three-clump galaxies using $p_3 \text{ clumps} > 0.75$, 71 four-clump galaxies using $p_4 \text{ clumps} > 0.70$, and 263 galaxies with more than four clumps using $p_{>4} \text{ clumps} > 0.70$. Alternatively, these data may be used to create more general samples of clumpy galaxies with few clumps and many clumps. A sample of 989 “few clumps” galaxies can be made using $(p_1 \text{ clump} + p_2 \text{ clumps}) > 0.5$ and 2,910 “many clumps” galaxies using $(p_3 \text{ clumps} + p_4 \text{ clumps} + p_{>4} \text{ clumps}) > 0.5$.

7. ANALYSIS

7.1. Demographics of morphology

Summarize the broad trends that are seen regarding the fraction of galaxies with various morphologies, how that relates to color, size, etc. Briefly discuss results as compared with literature and theory.

7.2. Comparing GZH morphologies to other catalogs

Table 13. Suggested thresholds for selecting morphological samples from Galaxy Zoo: Hubble.

No.	Task	Previous task(s)	Vote fraction threshold $N_{\text{task}} \geq 20$
01	smooth or features	—	—
02	edge on	01,12	$p_{\text{clumpy,no}} > 0.30$
03	bar	01,12,02	$p_{\text{pedgeon,no}} > 0.25$
		01,12,16,15	$p_{\text{clumpy spiral}} > 0.65$
04	spiral arms	01,12,02	$p_{\text{pedgeon,no}} > 0.25$
		01,12,16,15	$p_{\text{clumpy spiral}} > 0.65$
05	bulge prominence	01,12,02	$p_{\text{pedgeon,no}} > 0.25$
		01,12,16,15	$p_{\text{clumpy spiral}} > 0.65$
06	odd yes/no	—	—
07	rounded	01	$p_{\text{smooth}} > 0.70$
08	odd feature	06	$p_{\text{odd,yes}} > 0.50$
09	bulge shape	01,12,02	$p_{\text{pedgeon,yes}} > 0.40$
10	arms winding	01,12,02,04	$p_{\text{spiral,yes}} > 0.25$
11	arms number	01,12,02,04	$p_{\text{spiral,yes}} > 0.25$
12	clumpy	01	$p_{\text{features}} > 0.23$
13	bright clump	01,12,16	$p_{\text{one clump}} < 0.40$
14	bright central clump	01,12,16,13	$p_{\text{bright clump,yes}} > 0.50$
15	clump arrangement	01,12,16	$p_{\text{multiple clumps}} > 0.45$
16	clump count	01,12	$p_{\text{clumpy,yes}} > 0.80$
17	clumps symmetrical	01,12	$p_{\text{clumpy,yes}} > 0.80$
18	clumps embedded	01,12	$p_{\text{clumpy,yes}} > 0.80$

All of the Legacy surveys included in the GZH imaging have had morphological catalogs previously published; these catalogs have significant differences in the number of galaxies, size and magnitude limits, classification scheme, and the methods used for measuring morphology. These catalogs have been cross-matched to GZH to compare the results; this is not presented as an endorsement of any particular method, but as an exploration of the strengths and weaknesses of the GZ crowdsourced catalogs as compared to products made with machine learning, automatic fits, and expert visual classification.

The types and accuracies of morphological classification strongly depend on the sample and methods being used. In an attempt to make a consistent comparison between different techniques, galaxies are broadly grouped into three categories: bulge-dominated/elliptical/smooth, disk-dominated/spiral, and irregular/clumpy. These categories are compared to two parameters in GZH: $p_{\text{features,best}}$, which is designed to identify smooth (elliptical) galaxies, and p_{odd} , which is designed to identify deviations from well-formed spirals or S0s and which constitutes a “catch-all” for the variety of asymmetric morphologies that can constitute an irregular galaxy.

Morphologies for GEMS galaxies were measured by Häußler et al. (2007), who use single-component Sérsic fits to the F850LP imaging. This analysis uses parameters from the GALFIT code, which Häußler et al. (2007) evaluated as more reliable than GIM2D for GEMS due to the ability to fit multiple galaxies in crowded fields. A 1'' positional match for the GEMS galaxies in Table 9 in Häußler et al. (2007) to the GZH sample gives 8,846 galaxies in both Häußler et al. (2007) and GZH. The main morphological parameter in the automated catalog is the Sérsic index n defining the radial surface brightness profile. “Elliptical” galaxies are selected by $n > 2.5$ and “spirals” by $n > 2.5$. There is no automatic measurement of irregular or clumpy structure in this catalog.

AEGIS galaxies were morphologically classified using non-parametric measurements by Lotz et al. (2008). This method uses a combination of the Gini coefficient (G), which measures the relative inequality in pixel brightness, and M_{20} , the second-order moment of the brightest 20% of the light (Lotz et al. 2004). A linear combination of G and M_{20} delineates their three broad categories of galaxy morphology: E/S0/Sa (“elliptical”), Sb/Sc/Ir (“spiral”), and mergers (“irregular”). A 1'' positional match on AEGIS and GZH yields 4,031 galaxies with reliably-measured morphologies and $S/N > 3$ in both V - and I -bands.

Galaxies in both of the GOODS fields down to a limit of $z_{AB} = 22.5$ were visually classified by a single expert (R.S. Ellis), inspecting both z -band and composite Viz color images (Bundy et al. 2005). These morphologies are assigned a numerical value based on categories in Brinchmann et al. (1998); the corresponding morphologies used are “elliptical” (classes 0,1,2), “spirals” (classes 3,4,5), and “irregular” (classes 6,7,8). A 0.5'' matched radius yields 2,435 galaxies (1300 in GOODS-N, 1135 in GOODS-S) in both Bundy et al. (2005) and GZH.

COSMOS galaxies have multiple published datasets automatically classifying their morphologies, all using a variation of non-parametric measurements. Cassata et al. (2007) use a combination of concentration (C), asymmetry (A), G , and M_{20} (Cassata et al. 2005) to classify all galaxies with $m_{I,\text{petro}} < 25$, and use an empirical division based on several hundred training images to assign galaxies to discrete morphological categories. A similar method is employed by Tasca (2011), using the same non-parametric indices but with a different method of calculating the Petrosian radius and total light profile. They employ a nearest-neighbors method is used to assign morphological categories for the entire sample based on a small training set. Scarlata et al. (2007, ZEST) use C , A , G , M_{20} , the galaxy ellipticity (ϵ), and Sérsic index (n) to quantify the galaxy shapes; a principal component analysis is used to assign galaxies to

discrete morphological categories. The categories in all three methods are split into ellipticals, spirals, and peculiar/irregulars. A 0.5'' radius search on GZH matches to 76,241 galaxies in Cassata et al. (2007), 76,608 in Tasca (2011), and 77,425 in Scarlata et al. (2007).

Figure 10 shows the proportion of galaxies as split by their automated/expert visual morphologies for each of the six catalogs matched to GZH. The relation between GZH and the automated/expert morphologies is shown to vary significantly for different surveys — this may be due to intrinsic differences in the galaxies, in the techniques used to measure morphology, or both. The distribution of $p_{\text{features,best}}$ for AEGIS galaxies is essentially flat for spirals, showing almost no difference in proportion at the highest and lowest ends. Early-type galaxies are at their highest proportion at $p_{\text{features,best}} \sim 0$, but constitute only 40% of the galaxies at most. In contrast, GOODS galaxies at low $p_{\text{features,best}}$ are dominated by early-types, although spiral and irregular galaxies have comparable sizes as low as $p_{\text{features,best}} \sim 0.2$. In GEMS galaxies, the impact of irregular or peculiar galaxies is not measured; splitting on $n = 2.5$ gives an essentially flat proportion of ellipticals to spirals at $p_{\text{features,best}} > 0.3$. Visual inspection of images of galaxies where both $p_{\text{features,best}}$ and n are high show that the majority are obvious spirals but with prominent bulges, indicating that the single-component Sérsic fit is likely choosing too small of an effective radius and missing the extended disk structure for a large population of galaxies.

Even within the same sample of galaxies in COSMOS, different techniques of measuring morphology show significant differences. Both Cassata et al. (2007) and Tasca (2011) have higher proportions of early-type galaxies at $p_{\text{features,best}} \sim 0$, but constitute less than half the sample in both cases. The majority of all galaxies in Scarlata et al. (2007), in contrast, are spirals; oddly, the *highest* proportions of spirals are found at the lowest values of $p_{\text{features,best}}$. The decrease in spiral galaxies at higher $p_{\text{features,best}}$ is almost entirely balanced by an increase in irregulars. Early-types have a small bump near $p_{\text{features,best}} \sim 0.15$, but never constitute more than 10% of the sample.

The second set of plots in Figure 10 indicates that p_{odd} is largely an effective method for separating irregular and/or peculiar galaxies from spirals. Despite the somewhat vague wording of the “*anything odd?*” question in GZH, the AEGIS, COSMOS, and GOODS all show a marked increase in the irregular fraction increasing with p_{odd} . Any threshold value for distinguishing between the two, however, depends strongly on survey/redshift range.

As the data shown in Figure 10 cover a wide range of redshifts and sizes, a volume-limited sample of galaxies (or at least binning by redshift) is likely a much more

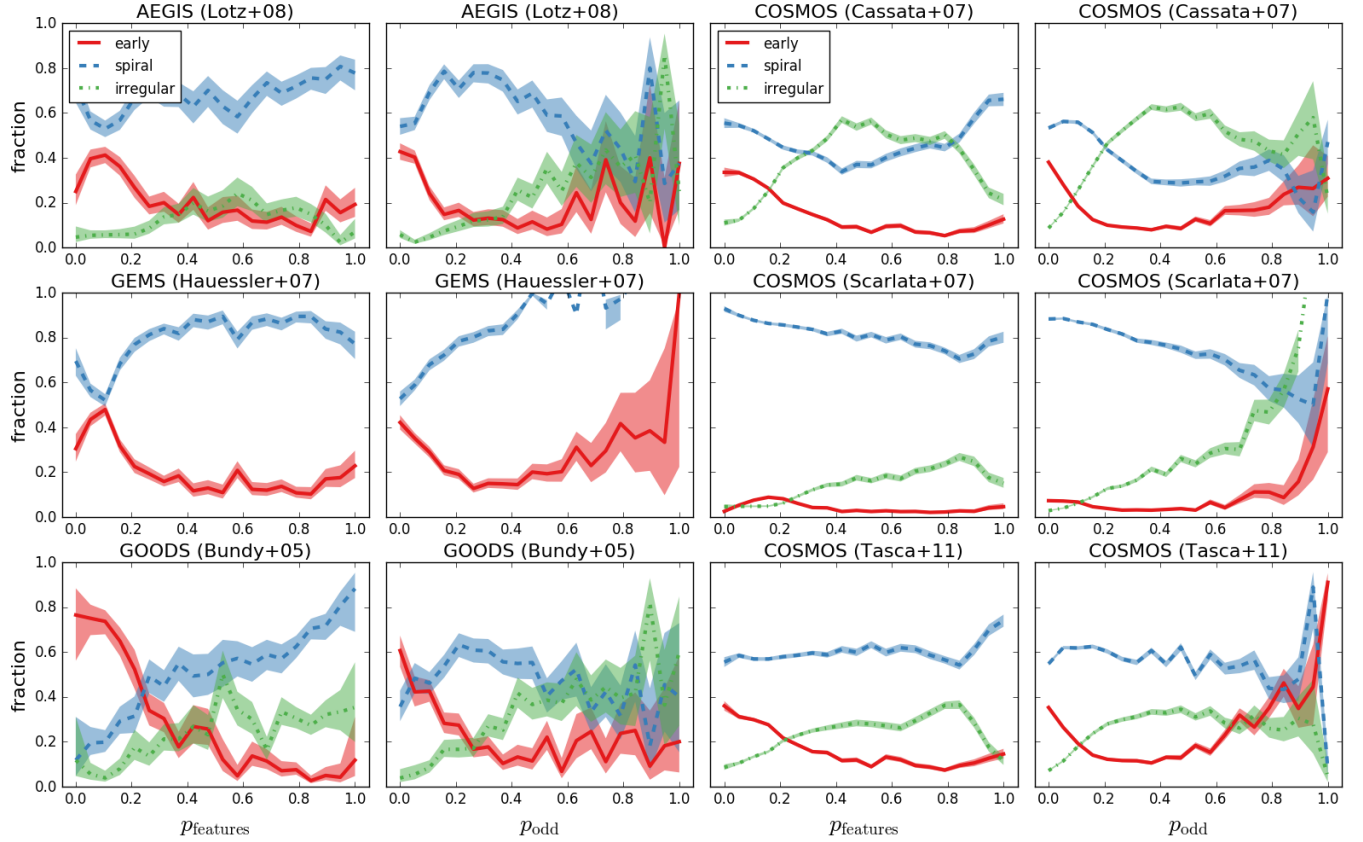


Figure 10. Distributions of morphological parameters for galaxies matched in GZH and other published catalogs, split by survey (AEGIS, COSMOS, GEMS, and GOODS). The first and third columns show the fraction of overall galaxies in the matched samples, split by their published morphologies as a function of the GZH $p_{\text{features,best}}$. The corresponding second and fourth columns show data for the same galaxies as a function of p_{odd} . Confidence intervals for each binned fraction in the bin are calculated for a binomial population (Cameron 2011).

appropriate comparison. While detailed analysis is left to a further paper, we note that there is no strong change in the proportion of galaxies when binning by redshift intervals of $\Delta z = 0.2$ out to $z = 1.0$.

8. SUMMARY

This paper presents the catalog release for the Galaxy Zoo: Hubble project, which uses crowdsourced visual classifications to measure galaxy morphologies. The first two phases of Galaxy Zoo (Lintott et al. 2011; Willett et al. 2013) used images of low-redshift galaxies from SDSS; this is the first phase of the project with space-based images of high-redshift targets (in addition to the Galaxy Zoo: CANDELS collaboration; Simmons et al., submitted). The final sample includes classifications for 181,101 images generated from 150,771 unique galaxies. Galaxies were selected from a brightness-limited sample from multiple Legacy surveys using the Advanced Camera for Surveys on the Hubble Space Telescope, including AEGIS, GEMS, GOODS-N, GOODS-S, and COSMOS. The catalog also includes classifications for 51,861 Sloan Digital Sky Survey images in Stripe 82 at relatively low redshift; these serve both as a low-redshift

anchor for cosmological studies and a potential comparison for the different epochs of classification between GZH and Galaxy Zoo 2 (Willett et al. 2013).

The data for the GZH catalogs has been extensively tested and reduced. The dominant effect is a known bias against identifying disky and asymmetric sub-structures at either low resolution or surface brightness. This can be the result either of genuinely small or dim galaxies, or a perceived effect from observing galaxies at further distances (higher redshift). To calibrate this *without* potentially overcorrecting for the genuine morphological evolution of galaxies over cosmic time, the GZH project uses SDSS images of low-redshift galaxies, processes them to appear as if they were at higher redshift, and classifies them through the GZH interface in an identical fashion. The resulting change in p_{features} as a function of z, μ is applied as a multiplicative correction to the top-level vote fractions for $\sim 50\%$ of the GZH galaxies.

Galaxies in GZH show significant changes in the disk/elliptical fraction as a function of redshift, along with an increasing number of galaxies dominated by smaller clumps and presumed to be in the process of building up their baryonic mass through a combina-

tion of hierarchical merging and in-situ star formation. While the majority of scientific interpretation is left to future work, this paper confirms the decrease in observed bar fraction with increasing redshift (Melvin et al. 2014) and identify a new way for identifying clumpy galaxies as a function of clump multiplicity.

The full data tables for the catalogs can be accessed in machine-readable form from both the journal and at <http://data.galaxyzoo.org>.

We thank Meg Schwamb and the ASIAA for hosting the “Citizen Science in Astronomy” workshop, 3–7 Mar 2014 in Taipei, Taiwan, at which some of this analysis was done. We also thank Jennifer Lotz for sharing her $G\text{-}M_{20}$ measurements for the AEGIS sample.

This project made heavy use of the Astropy packages in Python (Astropy Collaboration et al. 2013), the seaborn plotting package (Waskom et al. 2015), and astroML (Vanderplas et al. 2012). Modified code from Nick Wherry and David Schlegel was used to create the JPG images.

This work is based on (GO-10134, GO-09822, GO-09425.01, GO-09583.01, GO-9500) program observations with the NASA/ESA Hubble Space Telescope, obtained at the Space Telescope Science Institute, which is operated by the Association of Universities for Research in Astronomy, Inc., under NASA contract NAS 5-26555.

Funding for the SDSS and SDSS-II has been provided by the Alfred P. Sloan Foundation, the Participating Institutions, the National Science Foundation, the U.S. Department of Energy, the National Aeronautics and Space Administration, the Japanese Monbukagakusho, the Max Planck Society, and the Higher Education Funding Council for England. The SDSS website is <http://www.sdss.org/>.

The SDSS is managed by the Astrophysical Research Consortium for the Participating Institutions. The Participating Institutions are the American Museum of Natural History, Astrophysical Institute Potsdam, University of Basel, University of Cambridge, Case Western Reserve University, University of Chicago, Drexel University, Fermilab, the Institute for Advanced Study, the Japan Participation Group, Johns Hopkins University, the Joint Institute for Nuclear Astrophysics, the Kavli Institute for Particle Astrophysics and Cosmology, the Korean Scientist Group, the Chinese Academy of Sciences (LAMOST), Los Alamos National Laboratory, the Max-Planck-Institute for Astronomy (MPIA), the Max-Planck-Institute for Astrophysics (MPA), New Mexico State University, Ohio State University, University of Pittsburgh, University of Portsmouth, Princeton University, the United States Naval Observatory and the University of Washington.

REFERENCES

- Abraham R. G., van den Bergh S., Nair P., 2003, ApJ, 588, 218
 Astropy Collaboration et al., 2013, A&A, 558, A33
 Baillard A. et al., 2011, A&A, 532, A74
 Bamford S. P. et al., 2009, MNRAS, 393, 1324
 Bamford S. P., Rojas A. L., Nichol R. C., Miller C. J., Wasserman L., Genovese C. R., Freeman P. E., 2008, MNRAS, 391, 607
 Barden M., Häußler B., Peng C. Y., McIntosh D. H., Guo Y., 2012, MNRAS, 422, 449
 Barden M., Jahnke K., Häußler B., 2008, ApJS, 175, 105
 Beckwith S. V. W. et al., 2006, AJ, 132, 1729
 Behrendt M., Burkert A., Schartmann M., 2016, ApJL, 819, L2
 Bertin E., Arnouts S., 1996, A&AS, 117, 393
 Brinchmann J. et al., 1998, ApJ, 499, 112
 Bundy K., Ellis R. S., Conselice C. J., 2005, ApJ, 625, 621
 Caldwell J. A. R. et al., 2008, ApJS, 174, 136
 Cameron E., 2011, PASA, 28, 128
 Cameron E., Carollo C. M., Oesch P. A., Bouwens R. J., Illingworth G. D., Trenti M., Labb   I., Magee D., 2011, ApJ, 743, 146
 Cardamone C. N. et al., 2010, ApJS, 189, 270
 Cassata P. et al., 2005, MNRAS, 357, 903
 Cassata P. et al., 2007, ApJS, 172, 270
 Cheung E. et al., 2015, MNRAS, 447, 510
 Chevance M., Weijmans A.-M., Damjanov I., Abraham R. G., Simard L., van den Bergh S., Caris E., Glazebrook K., 2012, ApJL, 754, L24
 Conselice C. J., 2003, ApJS, 147, 1
 Conselice C. J., 2014, ARA&A, 52, 291
 Darg D. W. et al., 2010, MNRAS, 401, 1552
 Davis M. et al., 2007, ApJL, 660, L1
 de Vaucouleurs G., 1959, Handbuch der Physik, 53, 275
 Dressler A., 1980, ApJ, 236, 351
 Elmegreen D. M., Elmegreen B. G., 2014, ApJ, 781, 11
 Elmegreen D. M., Elmegreen B. G., Ferguson T., Mullan B., 2007, ApJ, 663, 734
 Elmegreen D. M., Elmegreen B. G., Marcus M. T., Shahinyan K., Yau A., Petersen M., 2009, ApJ, 701, 306
 Elmegreen D. M., Elmegreen B. G., Rubin D. S., Schaffer M. A., 2005, ApJ, 631, 85
 F  rster Schreiber N. M., Shapley A. E., Erb D. K., Genzel R., Steidel C. C., Bouch   N., Cresci G., Davies R., 2011, ApJ, 731, 65
 Freeman P. E., Izbicki R., Lee A. B., Newman J. A., Conselice C. J., Koekemoer A. M., Lotz J. M., Mozena M., 2013, MNRAS, 434, 282
 Galloway M. A. et al., 2015, MNRAS, 448, 3442
 Genel S. et al., 2014, MNRAS, 445, 175
 Giavalisco M. et al., 2004, ApJL, 600, L93
 Griffith R. L. et al., 2012, ApJS, 200, 9
 Grogin N. A. et al., 2011, ApJS, 197, 35
 Guo Y. et al., 2015, ApJ, 800, 39
 H  au  ler B. et al., 2007, ApJS, 172, 615
 Hinshaw G. et al., 2013, ApJS, 208, 19
 Hopkins P. F. et al., 2010, ApJ, 715, 202
 Hubble E. P., 1926, ApJ, 64, 321
 Hubble E. P., 1936, Realm of the Nebulae. Yale University Press
 Ilbert O. et al., 2013, A&A, 556, A55

Table A1. Correctable fractions for the top-level task in GZH in the GOODS shallow-depth (2-epoch) images.

	GOODS-N	GOODS-S	Total
Correctable	748	514	1,262
Lower limit	526	1,143	1,669
No Correction Needed ($z \leq 0.3$)	267	267	534
NEI	851	2,670	3,521
No Redshift Information	159	319	478
Total	2,551	4,913	7,464

- Johnson L. C. et al., 2015, ApJ, 802, 127
 Kartaltepe J. S. et al., 2015, ApJS, 221, 11
 Lackner C. N., Gunn J. E., 2012, MNRAS, 421, 2277
 Land K. et al., 2008, MNRAS, 388, 1686
 Law D. R., Shapley A. E., Steidel C. C., Reddy N. A., Christensen C. R., Erb D. K., 2012a, Nature, 487, 338
 Law D. R., Steidel C. C., Shapley A. E., Nagy S. R., Reddy N. A., Erb D. K., 2012b, ApJ, 745, 85
 Lintott C. et al., 2011, MNRAS, 410, 166
 Lintott C. J. et al., 2008, MNRAS, 389, 1179
 Lotz J. M. et al., 2008, ApJ, 672, 177
 Lotz J. M., Primack J., Madau P., 2004, AJ, 128, 163
 Lupton R., Blanton M. R., Fekete G., Hogg D. W., O'Mullane W., Szalay A., Wherry N., 2004, PASP, 116, 133
 Mandelker N., Dekel A., Ceverino D., DeGraf C., Guo Y., Primack J., 2015, ArXiv e-prints, 1512.08791
 Masters K. L. et al., 2011, MNRAS, 411, 2026
 Melvin T. et al., 2014, MNRAS
 Momcheva I. G. et al., 2015, ArXiv e-prints, 1510.02106
 Mortlock A. et al., 2013, MNRAS, 433, 1185
 Nair P. B., Abraham R. G., 2010, ApJS, 186, 427
 Peng C. Y., Ho L. C., Impey C. D., Rix H.-W., 2002, AJ, 124, 266
 Rix H.-W. et al., 2004, ApJS, 152, 163
 Sandage A., 1961, The Hubble atlas of galaxies. Carnegie Institute of Washington
 Scarlata C. et al., 2007, ApJS, 172, 406
 Schawinski K. et al., 2014, MNRAS, 440, 889
 Schaye J. et al., 2015, MNRAS, 446, 521
 Scoville N. et al., 2007, ApJS, 172, 1
 Silk J., Mamon G. A., 2012, Research in Astronomy and Astrophysics, 12, 917
 Simard L., Mendel J. T., Patton D. R., Ellison S. L., McConnachie A. W., 2011, ApJS, 196, 11
 Simmons B. D. et al., 2013, MNRAS, 429, 2199
 Simmons B. D. et al., 2014, MNRAS, 445, 3466
 Skibba R. A. et al., 2012, MNRAS, 423, 1485
 Strauss M. A. et al., 2002, AJ, 124, 1810
 Taniguchi Y. et al., 2007, ApJS, 172, 9
 Tasca L. A. M., 2011, VizieR Online Data Catalog, 7265
 Toomre A., Toomre J., 1972, ApJ, 178, 623
 van den Bergh S., 1976, ApJ, 206, 883
 Vanderplas J., Connolly A., Ivezić Ž., Gray A., 2012, in Conference on Intelligent Data Understanding (CIDU), pp. 47–54
 Vogelsberger M. et al., 2014, MNRAS, 444, 1518
 Waskom M. et al., 2015, seaborn: v0.6.0 (june 2015)
 Willett K. W. et al., 2013, MNRAS, 435, 2835
 Willett K. W. et al., 2015, MNRAS, 449, 820
 Williams R. E. et al., 1996, AJ, 112, 1335
 Wright E. L., 2006, PASP, 118, 1711
 York D. G. et al., 2000, AJ, 120, 1579

APPENDIX

A. GOODS SHALLOW DEPTH DATA

GZH used both 5-epoch and 2-epoch sets of data to construct the GOODS set of images. The 11,157 full depth 5-epoch images are used in the main catalog; the classifications for the 7,464 shallow depth 2-epoch images are offered as a supplementary table. This section analyzes the effect of image depth on the ability of the GZ users to identify features or disk structure in the images.

A.1. Comparing shallow and full depth morphologies

Of the 11,157 galaxies in the GOODS-N and GOODS-S full depth sample, 4,461 of these are in the shallow-depth sample. Figure A1 shows a strong correlation between p_{features} for both sets of images. The mean change in p_{features} from the shallow to full depth images $p_{\text{features,full}} - p_{\text{features,shallow}} \equiv \Delta p = 0.00$, with a standard deviation of $\sigma = 0.17$. While there is some variance in Δp in the whole sample, the change is usually small and not often significant enough to change a morphological classification. Defining a clean sample of disk galaxies as those with $p_{\text{features,best}} > 0.8$, elliptical galaxies as those with $p_{\text{smooth,best}} < 0.2$, and intermediate as those in between, 75% of the sample would not change morphology. Of the remaining 25% that would change morphology, only 0.3% (representing 10 galaxies total) drastically change morphology from smooth to featured or visa versa, while the rest would transition to or from the “intermediate” morphology. Details can be seen in Table A2 and examples of images representing the 9 possible changes (or lack of) in morphology are shown in Figures A2, A3, and A4.

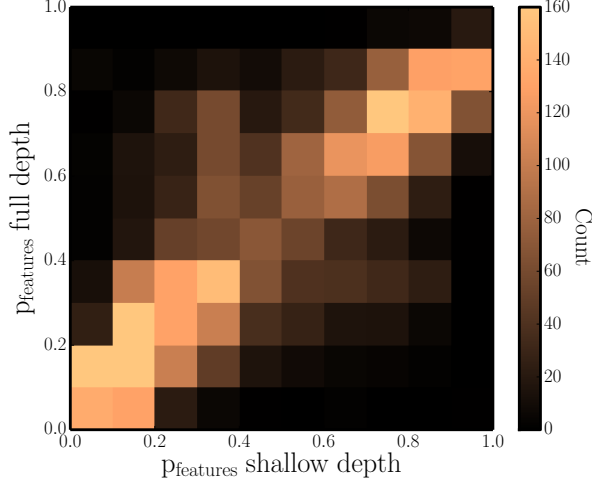


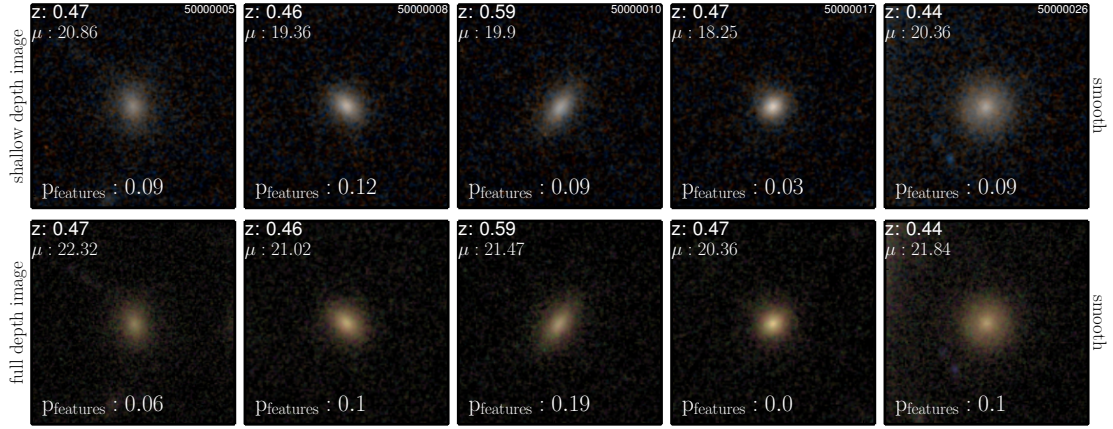
Figure A1. Distribution of p_{features} for the 4,461 GOODS galaxies with both shallow (2-epoch) and full-depth (5-epoch) images morphologically classified in GZH. For most galaxies, the value of p_{features} is consistent ($\Delta p_{\text{features}} < 0.2$) between depths. Examples of galaxies with sharp changes in p_{features} , as well as those with little to no change are shown in Figures A2-A4.

Table A2. Properties of galaxies whose morphologies changed or stayed the same in the shallow vs full images. Featured here is defined as $p_{\text{features,best}} > 0.8$, intermediate = $0.2 < p_{\text{features,best}} < 0.8$, smooth = $p_{\text{smooth,best}} < 0.2$.

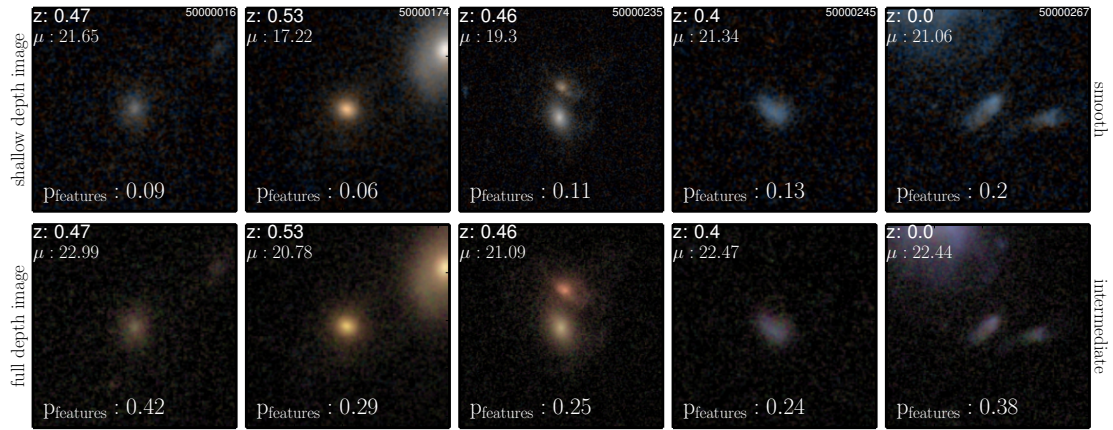
shallow to full morphology	N	%	$< \Delta p >$	$< z >$
smooth to smooth	758	17.0	-0.00	0.69
smooth to intermediate	367	8.2	0.18	0.69
smooth to featured	7	0.2	0.76	0.57
intermediate to smooth	214	4.8	-0.18	0.65
intermediate to intermediate	2,303	51.6	0.01	0.78
intermediate to featured	168	3.8	0.19	0.83
featured to smooth	3	0.1	-0.74	0.71
featured to intermediate	337	7.6	-0.18	0.68
featured to featured	301	6.8	-0.05	0.71
Total	4,461	100		

A.2. FERENGI analysis of p_{bar}

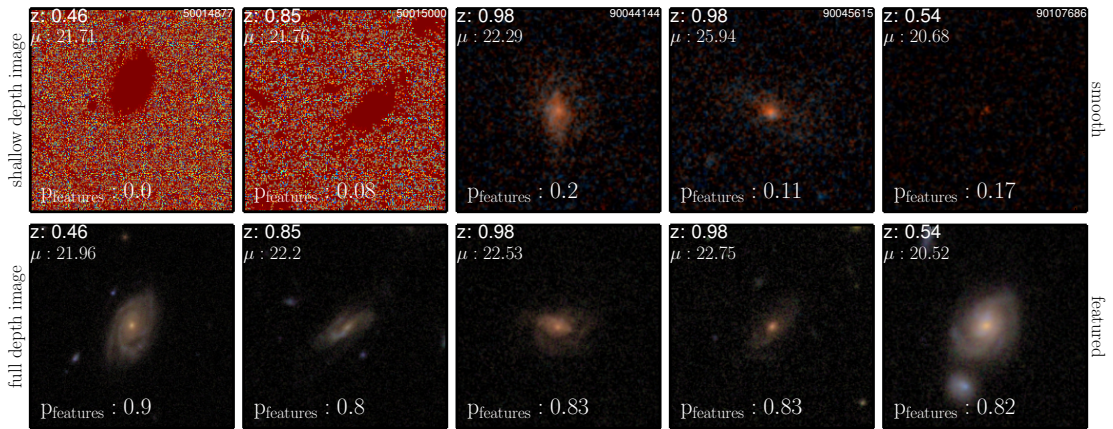
To determine the rate at which the vote fraction for any Task decreases with redshift or surface brightness, data from simulated FERENGI images were modeled with functions in discrete redshift and surface brightness bins (Section 4.3). A cut of $N > 10$ was placed on the number of votes to reduce the error in the vote fractions and ensure they were well-sampled before applying a fit to the data. This requirement was only met for Task 01, which significantly reduced the goodness-of-fit for the model functions as compared with to the smooth/features task. Here we show an example of results obtained for the bar Task. Figure A5 shows that both the low sample rate and the degree of scatter in each bin inhibit fitting a reliable function that predicts $p_{\text{bar},z=0.3}$. Table A5 summarizes the correction types for the FERENGI data ; 71% of the galaxies simulated did not meet the GZH requirements for well-sampled vote fractions for p_{bar} , as compared to 2% for p_{features} . Similar results were obtained for all higher-order Tasks in GZH, as described in Section 4.4.



[a]

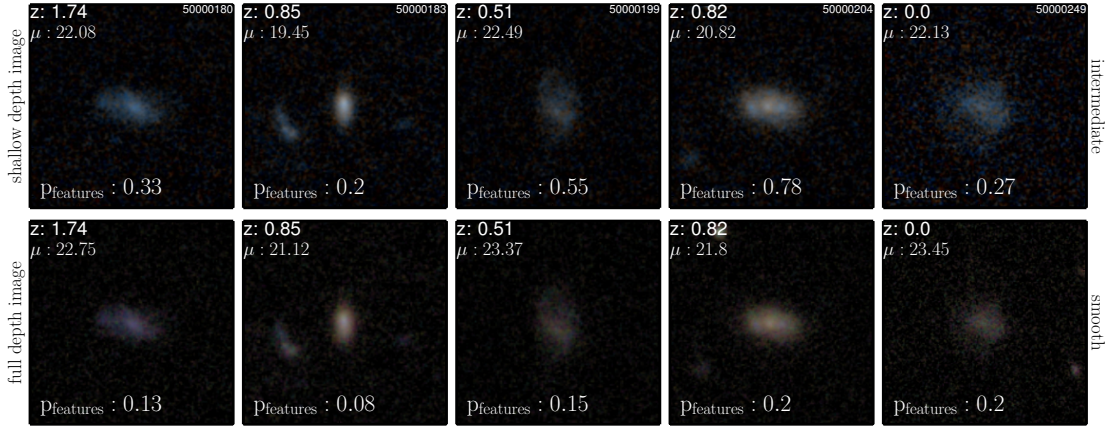


[b]

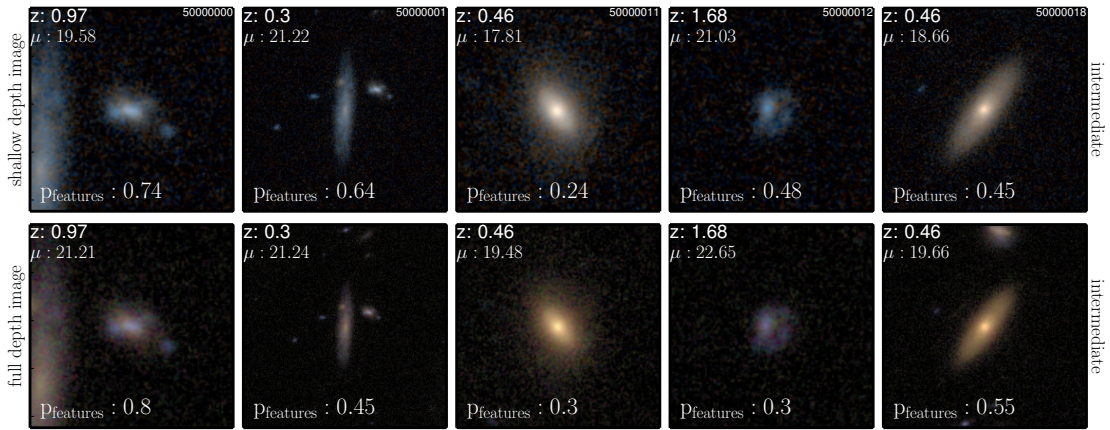


[c]

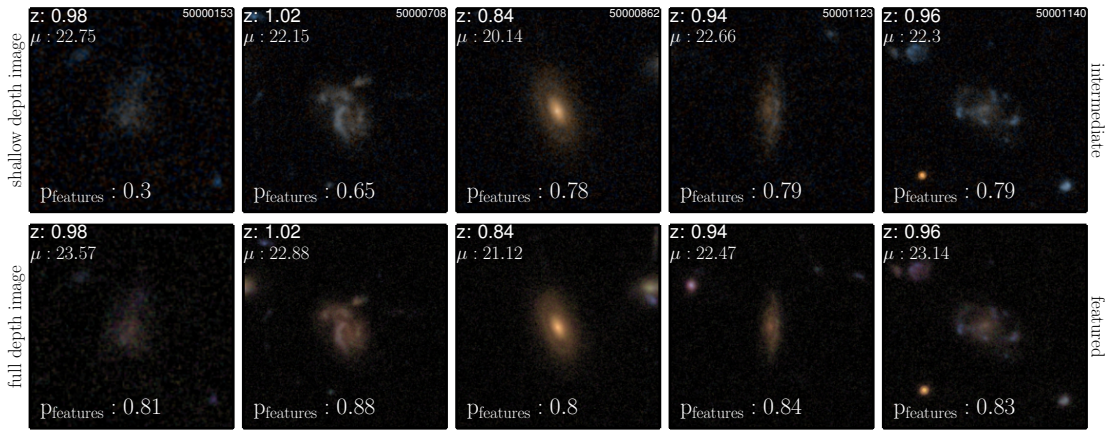
Figure A2. Galaxies whose shallow images were classified as smooth and full depth images were classified as smooth, intermediate, or featured.



[b]

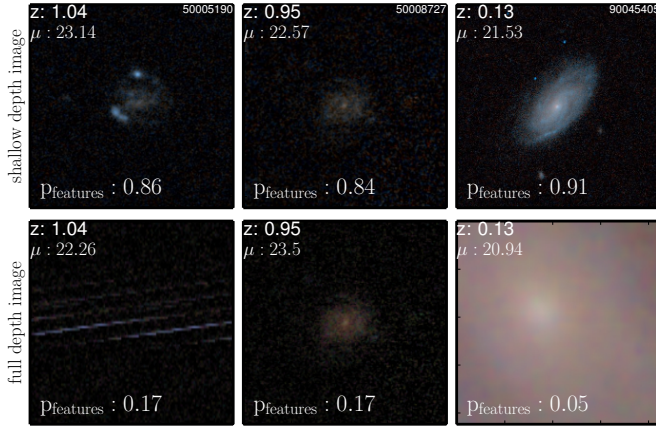


[b]

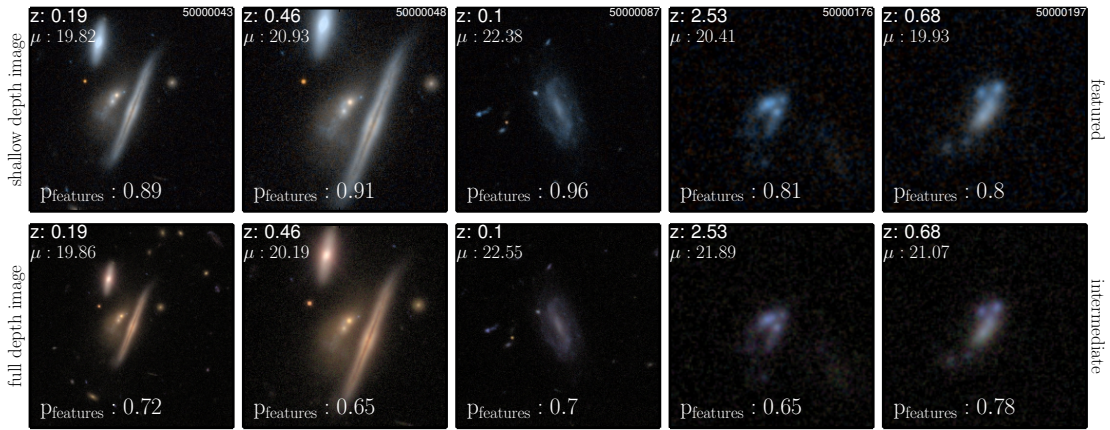


[b]

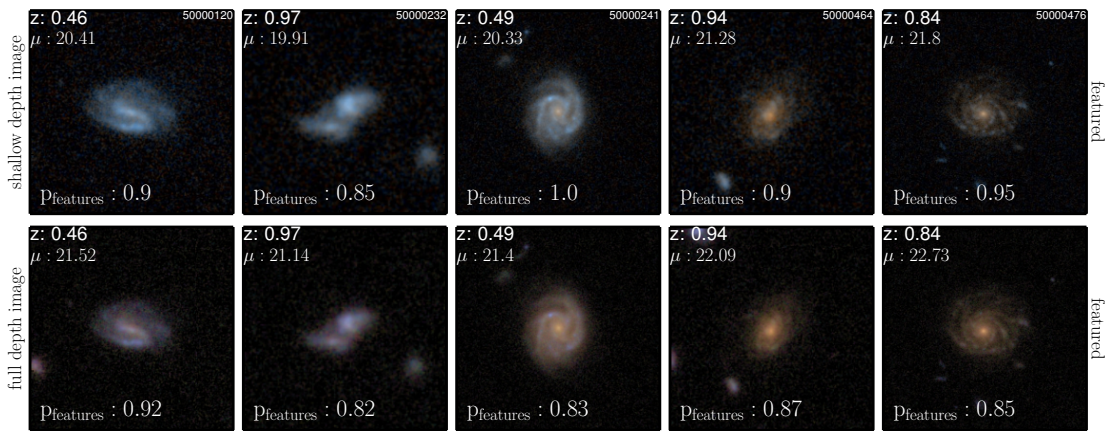
Figure A3. Galaxies whose shallow images were classified as intermediate and full depth images were classified as smooth, intermediate, or featured.



[b]



[b]



[b]

Figure A4. Galaxies whose shallow images were classified as featured and full depth images were classified as smooth, intermediate, or featured.

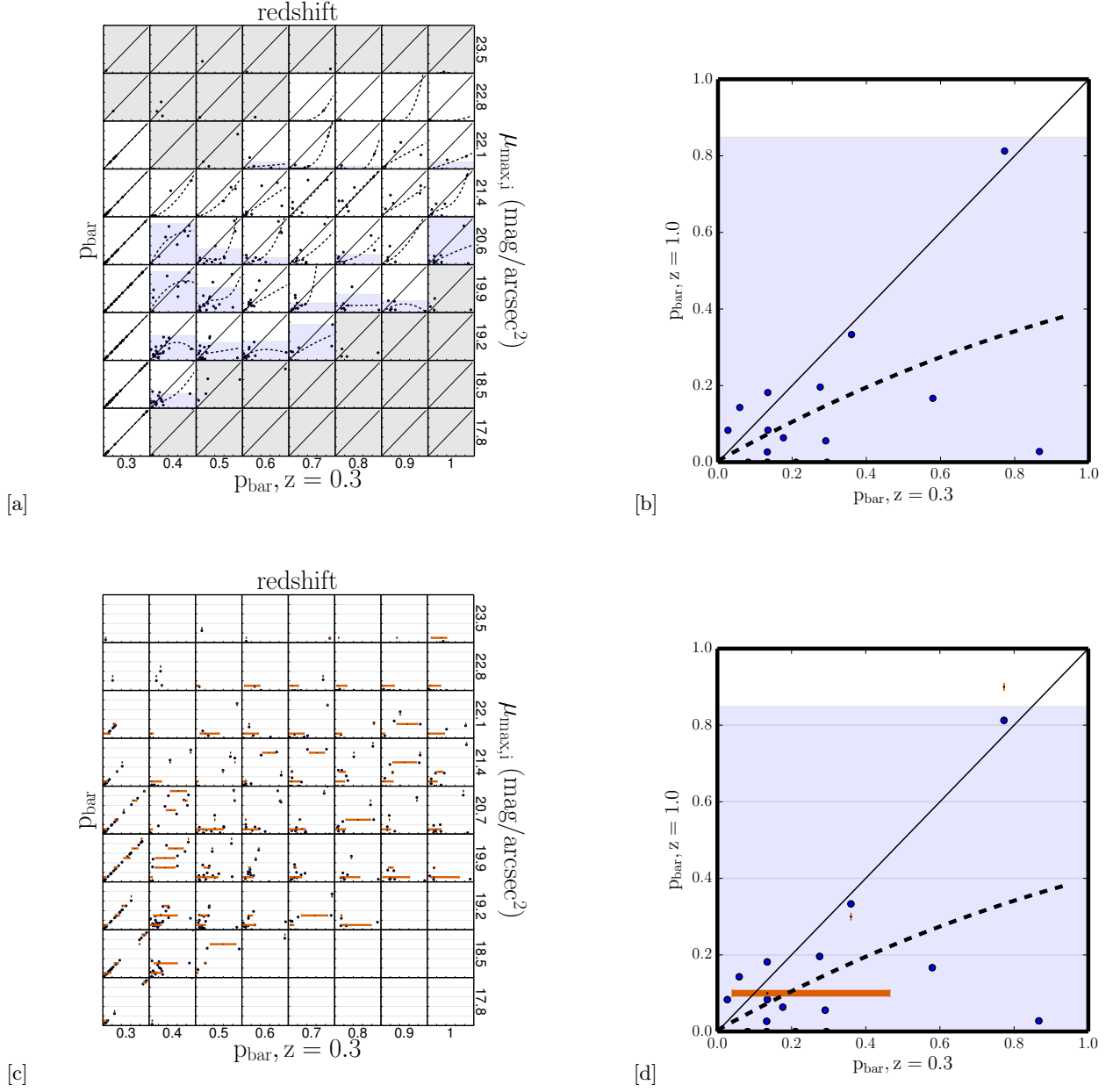


Figure A5. Similar to Figure 8, showing effects of redshift bias for 3,950 images in the FERENGI sample. [a]: Each point in a given redshift and surface brightness bin represents a unique galaxy. The y -axis in each bin is the p_{features} value of the image of that galaxy redshifted to the value corresponding to that redshift bin. The x -axis is the p_{features} value of the image of the same galaxy redshifted to $z = 0.3$. The dashed black lines represent the best-fit polynomials to the data in each square. The solid black line represents $p_{\text{features},z} = p_{\text{features},z=0.3}$. Regions in which there is a single-valued relationship between p_{features} at high redshift and at $z = 0.3$ are marked in white; those in which there is not are blue, and those with not enough data ($N < 5$) are gray. **The mean normalized χ^2 of 0.08 confirms that these polynomials are not good fits to the data, with no correction derived.** [b]: A larger version of the dark-outlined square in [a], containing FERENGI galaxies artificially redshifted to $z = 1.0$ and have surface brightnesses between $20.3 < \mu < 21.0$ (mag/arcsec 2). [c]: The same data as [a]. Each z, μ bin is divided into 4 sub-bins to determine the range of intrinsic $p_{\text{features},z=0.3}$ for a given range of observed $p_{\text{features},z}$ values. In each sub-bin, the orange bars represent the inner 80th percentiles of the data, the boundaries of which are the lower and upper limits of the debiased values. [d]: The same data as [b], but highlighting the upper and lower limit regions.

Table A3. Distribution of FERENGI images analysed in Figure A5. Correctable images had a single-valued relationship between their measured p_{bar} values at high and low redshifts (white regions in Figure A5). Galaxies with a lower-limit on p_{bar} had a non single-valued relationship (blue regions). NEI images had undetermined relationships due to a lack of data ($N < 5$) in their corresponding $z-\mu$ bins (gray regions). Only 17% (maximum) of FERENGI galaxies in the sample were considered “correctable”, which is not sufficient to compute a ζ function applicable to the Hubble data.

	N	%
Correctable	664	17%
Lower-limit	483	12%
NEI	2,803	71%
Total	3,950	100%